

# Interpreting broad emission-line variations II: Tensions between luminosity, characteristic size and responsivity

M. R. Goad<sup>1\*</sup> and K. T. Korista<sup>2</sup>

<sup>1</sup>*Department of Physics and Astronomy, College of Science and Engineering, University of Leicester, University Road, Leicester, LE1 7RH*

<sup>2</sup>*Department of Physics, Western Michigan University, Kalamazoo, Michigan 49008-5252, USA*

Received xxx; in original form June 2015

## ABSTRACT

We investigate the variability behaviour of the broad  $H\beta$  emission-line to driving continuum variations in the best-studied AGN NGC 5548. For a particular choice of BLR geometry,  $H\beta$  surface emissivity based on photoionization models, and using a scaled version of the 13 yr optical continuum light curve as a proxy for the driving ionizing continuum, we explore several key factors that determine the broad emission line luminosity  $L$ , characteristic size  $R_{\text{RW}}$ , and variability amplitude (i.e., responsivity)  $\eta$ , as well as the interplay between them.

For fixed boundary models which extend as far as the hot-dust the predicted delays for  $H\beta$  are on average too long. However, the predicted variability amplitude of  $H\beta$  provides a remarkably good match to observations except during low continuum states. We suggest that the continuum flux variations which drive the redistribution in  $H\beta$  surface emissivity  $F(r)$  do not on their own lead to large enough changes in  $R_{\text{RW}}$  or  $\eta_{\text{eff}}$ . We thus investigate dust-bounded BLRs for which the location of the effective outer boundary is modulated by the continuum level and the dust-sublimation and dust-condensation timescales. We find that in order to match the observed variability amplitude of broad  $H\beta$  in NGC 5548 a rather static outer boundary is preferred.

Intriguingly, we show that the most effective way of reducing the  $H\beta$  delay, while preserving its responsivity and equivalent width, is to invoke a smaller value in the incident ionizing photon flux  $\Phi_{\text{H}}$  for a given ionizing source–cloud radial distance  $r$ , than is normally inferred from the observed UV continuum flux and typical models of the continuum SED.

**Key words:** galaxies: active – galaxies: Seyfert – quasars: emission lines – methods: numerical

## 1 INTRODUCTION

Time variable continuum and broad emission-line studies (reverberation mapping) have demonstrated beyond doubt that the broad emission line region (hereafter BLR) in Active Galactic Nuclei (AGN) is both geometrically thick and highly stratified, with strong gradients in density and/or ionization state (e.g. Krolik et al. 1991; Clavel et al. 1991; Peterson et al. 2002, and references therein). Observations of multiple UV and optical broad emission-lines in individual sources and which span a range in ionization potential indicate that the high ionization lines (HILs, e.g. N V, C IV,

He II) respond on the shortest timescales, while the low ionization lines, e.g. Mg II, Fe II and optical/IR recombination lines ( $H\alpha$ ,  $H\beta$ ,  $H\gamma$ , Pa  $\alpha$ ) respond on longer timescales (e.g., Peterson et al. 2002; Barth et al. 2013). If the continuum–emission-line delays relate simply to the separation between the continuum and emission-line forming regions, then the observed differences between the response timescales of individual lines suggest that lines of differing ionization potential preferentially form at different radial distances (implying a spatially extended BLR), with the HILs forming closer to the continuum source than the LILs.

More recently, dust reverberation studies place the dust emission just beyond the furthest reaches of the BLR, with delays somewhat larger than the largest delays measured for the LILs (Suganuma et al. 2004, 2006; Koshida et al. 2009,

\* E-mail: mg159@le.ac.uk

2014; Schnülle et al. 2013, 2015; Kishimoto et al. 2013). At smaller radii, the intense radiation field may contribute to cloud destruction (Mathews 1982), over-ionize the gas, or the surviving clouds may become continuum sources in this high pressure environment (Ferland and Rees 1988). Thus a picture of the BLR is emerging in which the BLR gas is bounded on its inner edge by continuum sources (i.e. the inner accretion disc), while at large radii the extinction of ionizing photons and the destruction of optically-thick emission lines by grains, causes the efficiency at which a particular emission-line forms to drop significantly (e.g. Netzer and Laor 1993).

For NGC 5548, in order to match the observed luminosities of the strong UV lines, photoionization model computations indicate that its BLR spans  $\sim 2$  decades in radial extent from  $\sim 1$ –100 light-days (Korista and Goad 2000; Kaspi and Netzer 1999).

While photoionization models alone can broadly constrain the radial extent of the BLR, information concerning the spatial distribution and kinematics of the BLR gas within the confines of these boundaries requires the additional information supplied by reverberation mapping of multiple broad emission-lines in individual sources. The most recent emission-line velocity–delay maps indicate evidence for inflow, outflow and circularised motion, often with evidence for more than one type of motion in a single source (Skjelboe et al. 2015; Grier et al. 2013; Pancoast et al. 2014b; Barth et al. 2011; Bentz et al. 2010; Denney et al. 2009, 2010). The prevailing view is that gas motion is generally virialised, a fact which has been usefully exploited in conjunction with BLR ‘size’ estimates to determine black hole masses for approaching nearly 60 nearby low luminosity AGN (see Bentz and Katz 2015 for the most recent compilation of reverberation mapped sources; Peterson et al. 2004, and references therein; Bentz et al. 2008, 2009a,b; Pancoast et al. 2012, 2014a, 2014b). However, the spatial distribution of the BLR gas is far harder to fathom. The 1-d response function  $\Psi'(\tau)$ , the function which maps the continuum variations on to the emission-line variations, alone is degenerate, with disparate geometries yielding broadly similar 1-d response functions (Welsh and Horne 1991; Pérez, Robinson and de la Fuente 1992), and the recovered 2-d response functions  $\Psi'(v, \tau)$  (or velocity–delay maps) are only now reaching sufficient fidelity to provide useful constraints on the gas distribution and kinematics (Grier et al. 2013; Pancoast et al. 2012, 2014a, 2014b; Bentz et al. 2010).

In this work, we explore the role of the BLR outer boundary in establishing an emission line’s luminosity, delay (lag), and variability amplitude (responsivity) in the presence of ionizing continuum variations, and identify the strong connection between these three quantities. The most up to date measurement of the size-luminosity relation for broad  $H\beta$  in nearby AGN suggests a relation of the form  $R_{\text{BLR}}(H\beta) \propto L_{\text{opt}}^\alpha$ , with  $\alpha \approx 0.5$  (Bentz et al. 2009; Bentz et al. 2013; Kilerci Eser et al. 2015). This scaling is a naive prediction of the simplest photoionization model calculations. The broad similarity between AGN spectra spanning a wide range in continuum source luminosity suggests that the physical conditions within the line-emitting gas are broadly similar from one object to the next. In that case, the ionization parameter  $U$  which relates the number of hydrogen ionizing photons  $Q_{\text{H}}$  to hydrogen gas number density  $n_{\text{H}}$  and

ionizing continuum source–cloud separation  $r$  through the relation  $U = Q_{\text{H}}/4\pi r^2 n_{\text{H}} c$ , then gives  $r \propto (Q_{\text{H}}/U n_{\text{H}})^{1/2}$ .

### 1.1 The BLR in NGC 5548 from correlated continuum–emission-line variability studies

UV spectroscopic monitoring of the best studied source, the nearby Seyfert 1 galaxy NGC 5548, reveals that the HILs undergo large amplitude short timescale variations. Indeed, the 1-d response functions for the HILs (N V, C IV, He II) are temporally unresolved on the shortest timescales, peaking at zero delay, and declining rapidly toward longer delays, with a mean response timescale of only a few days (e.g. Krolik et al. 1991; Clavel et al. 1991; Korista et al. 1995). By contrast, the amplitude of the response for the LILs (Mg II, Fe II) is much weaker, and their mean response timescales both larger and with large uncertainty (Clavel et al. 1991; Maoz et al. 1993; Vestergaard and Peterson 2005; Kuehn et al. 2008; Barth et al. 2013). Furthermore, the C III] inter-combination line, a line which is collisionally de-excited at high gas densities, also displays a smaller amplitude response and longer delays than the HILs suggesting that densities generally decrease toward larger BLR radii in this source. The amplitude and response timescales for the broad optical recombination lines are intermediate between those of the HILs and LILs (e.g. Peterson et al. 2002). For example, for broad  $H\beta$  the 1-d response function recovered from the 13 yr ground-based optical monitoring campaign on NGC 5548 is characterised by an absence of response on both short and long timescales, rising to a peak response on timescales of order 20 days, with a full-width at half-maximum (FWHM) of  $\approx 10$  days (e.g. Horne, Welsh and Peterson 1991; Cackett and Horne 2006). See paper I for a more detailed description of the 13 yr ground-based monitoring data on NGC 5548.

The simplest explanation for the differences in the measured delays for lines of differing ionization potential, is that the BLR in NGC 5548 is spatially extended and highly stratified, though the typical delays for the responding region appear to imply a far more compact BLR than photoionization models might suggest, and which remains a challenge in terms of balancing the energy budget for the strongest UV and optical recombination lines (Netzer 1985, Collin-Souffrin 1986). The absence of significant response for broad  $H\beta$  on the shortest timescales can be explained either by an absence of gas along the line of sight to the observer, implying a significant departure from spherical symmetry, for example a disc or bowl-like geometry, or by line of sight gas which is very optically-thick in the line, in which case the emission-line will emerge predominantly from the illuminated face of the cloud<sup>1</sup>.

Ferland et al. (1992), O’Brien et al. (1994), and Korista and Goad (2004) estimate that the fraction of Balmer line photons emerging from the illuminated face of typical BLR clouds lies in the range 80–100%. However, only a bowl-shaped BLR geometry can simultaneously account for the

<sup>1</sup> Dynamical modelling of reverberation mapping data taken for the optical recombination lines in a small number of nearby Seyfert 1 galaxies, indicates that the observed line emission for broad  $H\beta$  emerges preferentially from the illuminated face of the BLR clouds (e.g. Pancoast et al. 2014a).

absence of significant response in the line on both short and long timescales (Goad, Korista and Ruff 2012). For a bowl-shaped geometry, BLR gas is elevated above the disc mid-plane and gives rise to smaller time-delays for a fixed radial distance than would otherwise be expected for spherical or flattened BLR geometries. In the limit where gas lies along an iso-delay surface, the measured delay is independent of cloud-ionizing continuum source distance. For NGC 5548, a bowl-like model also has the significant advantage in that it reconciles the measured distance to the hot dust, as estimated from the delay between the optical and IR continuum bands ( $\tau \approx 50$  days, Suganuma et al. 2004) with photoionization calculations, which predict a minimum distance of  $\approx 100$  light-days for grain survival.

## 1.2 Factors influencing the emission-line responsivity

Goad and Korista (2014, hereafter paper 1) investigated the effect of geometric dilution on the amplitude of the emission-line response (the line responsivity  $\eta_{\text{eff}}$ ) and delay. Formally, the line responsivity, is the power-law index which relates the measured continuum and emission-line fluxes,  $f_{\text{cont}}$  and  $f_{\text{line}}$ , via

$$f_{\text{line}} \propto f_{\text{cont}}^{\eta_{\text{eff}}}. \quad (1)$$

$\eta_{\text{eff}}$  is a measurable quantity, and is normally estimated after first applying a small correction for the continuum-emission-line delays (e.g. Pogge and Peterson 1992), with due allowance for contaminating galaxy and narrow emission-line contributions to the continuum and broad emission-lines respectively.

The efficiency by which ionizing continuum photons are converted into emission line photons, the emission line EW, is related to the line responsivity according to

$$\frac{d \log EW}{d \log f_{\text{cont}}} = \eta_{\text{eff}} - 1. \quad (2)$$

The connection between the line responsivity and the line EW is thus made clear. For  $\eta_{\text{eff}} = 1$ , the  $EW(\text{line}) = \text{constant}$  with respect to the change in the incident continuum, and thus the reprocessing efficiency for a particular line is independent of (a finite change in) continuum level. Values of  $\eta_{\text{eff}} < 1$ , indicate that the line reprocessing efficiency diminishes with increased continuum flux (an intrinsic Baldwin effect for that line, e.g. Gilbert and Peterson 2003; Korista and Goad 2004; Goad, Korista and Knigge 2004; Goad and Korista 2014). While for  $\eta_{\text{eff}} > 1$ , the line reprocessing efficiency increases with increasing continuum flux.

In paper 1, Goad and Korista (2014) demonstrated that an alternative estimate of  $\eta_{\text{eff}}$  can be made using only the ratio of the variances of the line and continuum light-curves, as was first suggested by Krolik et al. (1991), once again after first applying a suitable correction for the contaminating galaxy and narrow-line components. Factors controlling the measured emission-line responsivity  $\eta_{\text{eff}}$  include : (i) the local gas reprocessing efficiency (Korista and Goad 2004, hereafter referred to as the local line responsivity  $\eta(r)$ ), (ii) the amplitude and characteristic timescale of the driving continuum light-curve, (iii) the BLR geometry and observer line

of sight orientation, and (iv) the duration of the monitoring experiment.

Previous studies indicated that the emission-line response was only weakly affected by geometric dilution (e.g. Gilbert and Peterson 2003). However, Goad and Korista (2014) showed that for geometries approaching the size expected for NGC 5548, geometric dilution could in fact be significant. In general the importance of geometric dilution depends upon the characteristic timescale  $T_{\text{char}}$  of the driving continuum light-curve in relation to the maximum delay of a given emission-line  $\tau_{\text{max}}(\text{line})$ .  $\tau_{\text{max}}(\text{line})$  is here defined to be the maximum time-delay for a given emission line for a particular geometry and observer line-of sight orientation. For  $T_{\text{char}} < \tau_{\text{max}}(\text{line})$ , the measured responsivity and delay, directly correlate with  $T_{\text{char}}$ .

To illustrate these effects, in paper 1 we modelled the radial surface emissivity distribution for the line emitting gas as a simple power-law in radius  $F(r) \propto r^\gamma$ , since under these conditions the local radial line responsivity  $\eta(r)$  is constant, both spatially and temporally (i.e.  $\eta(r) = -(\gamma/2) = \text{constant}$ ). Therefore, in this case the only factors which can influence the measured line responsivity are the campaign duration, amplitude and characteristic timescale of the driving continuum light-curve for a particular choice of BLR geometry and observer line-of-sight orientation. In all cases broad emission-line light-curves were determined using a locally-linear response approximation for a stationary BLR with fixed boundaries. Thus, the models explored in paper 1 were by design constructed to be time-steady. As such, the amplitude of the emission-line response and the responsivity-weighted size of the BLR will remain constant in time. Therefore, “breathing”, the observed positive correlation between BLR size and continuum state (Korista and Goad 2004; Goad, Korista and Knigge 2004; Cackett and Horne 2006; Bentz et al. 2007; Kilerci Eser et al. 2015), was not addressed.

Paper 1 also indicated that the measured emission-line responsivity and delay for a fixed  $T_{\text{char}}$ , show significant variation for BLRs differing only in their radial surface emissivity distribution and/or their spatial extent. Thus, if either the local surface emissivity distribution and/or the location of the BLR inner and outer boundaries were to vary with continuum level, we would expect to find significant changes in the measured responsivity and delay. For static BLR boundaries changes in the measured responsivity and delay require radial surface emissivity distributions that depart significantly from a simple power-law over the radial extent of the BLR. Breathing requires the emission-line responsivity to generally increase toward lower incident ionizing continuum fluxes or *equivalently larger BLR radii*. This ensures that the mean line formation radius will drop in low continuum states and rise in high continuum states as is observed. This requirement may be relaxed, if instead the BLR boundaries are allowed to adjust with continuum level, moving outwards/inwards as the continuum rises/falls (though not necessarily in lock-step). In practice, it may be that both are required to match the observed behaviour of the emission-lines in response to continuum variations.

Investigating the redistribution of the emission-line energy within the BLR, in the presence of incident continuum flux variations is the subject of the following contribution. In the context of model BLRs with both static and varying

boundaries (for a particular geometry and observer orientation), we here explore the nature of the broad emission-line response, its amplitude and delay, assuming a full non-linear response in the lines, and using radial surface emissivity distributions for the  $H\beta$  emission line determined from photoionization calculations. As we show in §2, these indicate significant departures from a simple powerlaw radial surface emissivity distribution over the radial extent of the fiducial BLR geometry. We compare model predictions to the 13-year light curve for broad  $H\beta$  in NGC 5548 (Peterson et al. 2002) to elucidate the physical factors that determine a particular emission line’s average luminosity, its response delay (‘lag’) and amplitude (‘responsivity’) – as well as the relationship between these three quantities.

This paper is structured as follows: In §2 we describe the fiducial BLR geometry for NGC 5548, onto which we project a Locally Optimally-emitting Clouds (hereafter LOC) model description for the radial surface emissivity distribution  $F(r)$ , constructed from photoionization calculations which use a continuum normalisation appropriate for this source. In §3 we drive the fiducial model as well as representative powerlaw models for the radial surface emissivity distribution, to produce broad  $H(\beta)$  emission-line light curves which we compare to the broad  $H(\beta)$  emission-line lightcurve as observed over 13 years of ground-based monitoring of NGC 5548. In §4 we examine the link between the emission line luminosity, emission line responsivity and emission-line delay, highlighting those physical affects which when present can act to enhance the  $H\beta$  luminosity and response amplitude at small BLR radii. In §5 we use simple toy models of a dust-bounded BLR to explore the nature of the BLR outer boundary, and its effect on the emission-line response amplitude and delay. In §6 we demonstrate the implications (in terms of the measured response amplitude and delay) for a dust-bounded BLR model for NGC 5548. We discuss and summarise the results in §7.

For the purposes of computing continuum and emission line luminosities and determining physical radial scales within the BLR, we adopt the redshift of NGC 5548,  $z=0.0172$ , and the following cosmological parameters:  $H_0 = 67.3 \text{ km s}^{-1} \text{ Mpc}^{-1}$ ,  $\Omega_m = 0.315$ ,  $\Omega_\Lambda = 0.685$ , with a corresponding luminosity distance to NGC 5548 of 77.6 Mpc (Ade et al. 2014).

## 2 A FIDUCIAL BLR MODEL

The fiducial BLR geometry has been described in detail elsewhere (e.g. Goad, Korista, and Ruff 2012; Goad and Korista 2014). This geometry was introduced as a means of connecting the outer accretion disc with the reservoir of gas that likely fuels the continuum source (i.e. the dusty torus). By introducing significant scale-height at large BLR radii (see also Collin et al. 2006) this geometry can reconcile the small dust-delays reported for NGC 5548 (Suganuma et al. 2004, 2006; Koshida et al. 2014), with the larger predicted distance at which robust graphite grains sublimate (Mor and Netzer 2012). In summary, the broad line-emitting gas occupies the surface of an approximately bowl-shaped region characterised in terms of a radially dependent scale height  $H$ , according to

$$H = \beta(r_x)^\alpha, \quad (3)$$

where  $r_x$  is the projected radial distance along the plane perpendicular to an observers line of sight (i.e.  $r_x = r \sin \phi$ ,  $r$  is the cloud source distance,  $\phi$  is the angle between the polar axis and the surface of the bowl), and  $\alpha, \beta$  control the rate at which  $H$  increases with  $r, \phi$ .<sup>2</sup> We choose a velocity field of the form

$$v_{\text{kep}}^2 = K \frac{r_x^2}{(r_x^2 + \beta^2 r_x^{2\alpha})^{3/2}}, \quad (4)$$

where  $v_{\text{kep}}$  is the local Keplerian velocity and  $K = GM_{\text{BH}}$ , where  $M_{\text{BH}}$  is the mass of the black hole. In the limiting case of a geometrically thin disc, (i.e.  $\beta = 0$ ), the velocity field reduces to that expected for simple planar Keplerian orbits. Significant radial motion, e.g., bulk radial motion or scale height dependent turbulence (Collin et al. 2006), may be included by introducing an azimuthal perturbation to the velocity field (see e.g. Goad, Korista and Ruff (2012), their equation 4.) We adopt  $\alpha = 2$  and a time-delay at the outer radius  $\tau(r = R_{\text{out}}) = (r - H)/c = 50$  days, chosen to match the dust-delay reported for the Seyfert 1 galaxy NGC 5548 (Suganuma et al. 2004, 2006; Koshida et al. 2014), yielding  $\beta = 1/150$ . We assume a black hole mass of  $10^8 M_\odot$ , similar to the best-estimate of MBH for this source derived from reverberation mapping experiments (Peterson and Wandel 2000). For the continuum normalisation appropriate for NGC 5548 the fiducial BLR geometry spans a radial distance of between 1.14–100 light-days. Here we set the BLR inner radius to 200 gravitational radii. However, differences of a factor a few in  $R_{\text{in}}$ , arising from differences in the adopted value of  $M_{\text{BH}}$  can be tolerated because in general (i) the radial surface emissivity distribution  $F(r)$  decreases at the smallest BLR radii for most lines, and (ii) the surface area of BLR clouds at small BLR radii is small. Taken together the contribution to the total line emission of gas located at small BLR radii is small (see §5.1). The BLR outer radius is here set by the distance at which robust graphite grains can survive. For the bowl inclination, we adopt  $i = 30$  degrees, close to the value reported for NGC 5548 by Pancoast et al. (2014b), a value considered to be typical of the expected inclination of type I objects.

### 2.1 Radial surface emissivity distributions

In paper I we adopted simple power-law radial surface emissivity distributions  $F(r) \propto r^\gamma$ , with power-law indices  $\gamma$  chosen to broadly match the range predicted by photoionization model calculations ( $-2 \leq \gamma \leq -1$ ). Under these conditions, the radial emission-line responsivity  $\eta(r)$  is constant both spatially and temporally  $\eta(r) = -(\gamma/2) = \text{constant}$  (we assume here, and throughout, that the incident ionizing continuum flux scales as  $r^{-2}$ ). In this contribution we use the

<sup>2</sup> The bowl-shaped surface is a zeroth order approximation of a BLR geometry in which the scale height is significant and increases with increasing radial distance. We do not exclude the possibility that line emitting gas exists “behind” the bowl surface (which may itself be patchy) at large physical depths, and which sees an extinguished ionizing continuum. The subsequent escape of such lines will depend upon the cloud distribution.

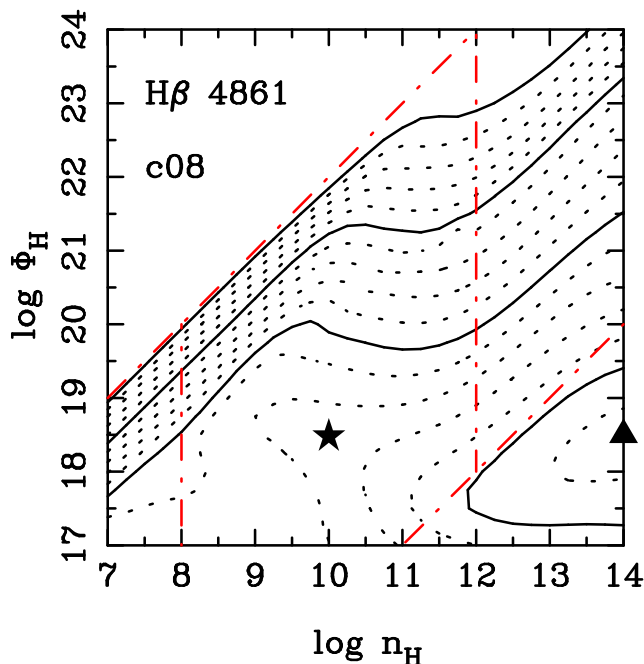


**Figure 1a.** Contours of predicted  $\log(EW)$  for broad  $H\beta$  referenced to the incident continuum flux at  $\lambda 1215\text{\AA}$  for full source coverage at each point in the grid, as a function of gas hydrogen density  $n_H$  and hydrogen-ionizing photon flux  $\Phi_H$ . The total hydrogen column density for each cloud in the grid is  $\log N_H(\text{cm}^{-2}) = 23$ . The smallest contour corresponds to  $0.1\text{\AA}$ , each solid line represents 1 decade, and dotted lines represent 0.2 dex intervals. Contours of  $\log(EW) < -1$  are not plotted (upper left quadrant). The solid star marks the old “standard BLR” parameters, the solid triangle the peak EW. The dot-dashed red lines indicate the range in  $\log Uc \equiv \log(\Phi_H/n_H)$  (diagonal lines) and  $\log n_H$  (vertical lines) used to compute the radial surface emissivity distribution (Figure 1b, upper panel).

radial surface emissivity distributions for individual lines as described in Goad, Korista and Ruff (2012).

In brief, we computed a grid of photoionization models assuming simple constant density slabs of gas with fixed constant total hydrogen column density  $\log N_H(\text{cm}^{-2}) = 23$ , solar abundances, and each with a direct view of the ionizing continuum source. Unless otherwise stated, here photoionization model calculations were performed with Cloudy, version C08.00 (Ferland, Korista and Verner 1997; Ferland et al. 1998), adopting a modified version of the Mathews and Ferland (1987) generic AGN continuum spectral energy distribution (see Goad, Korista, and Ruff 2012 for details). We note that while this incident continuum SED is likely softer (smaller X-ray/UV power ratio) than is expected in NGC 5548, these differences have relatively small effects on the predicted hydrogen line spectrum (Korista et al. 1997). Here, the incident continuum has been scaled to match an estimate for the mean ionizing continuum luminosity of NGC 5548,  $\log L_{\text{ion}}(\text{erg s}^{-1}) = 44.14$ , based on the Galactic extinction corrected mean UV flux at  $1350\text{\AA}$  measured during the 1993 HST monitoring campaign (Korista et al. 1995)<sup>3</sup>. For the adopted ionizing continuum shape and nor-

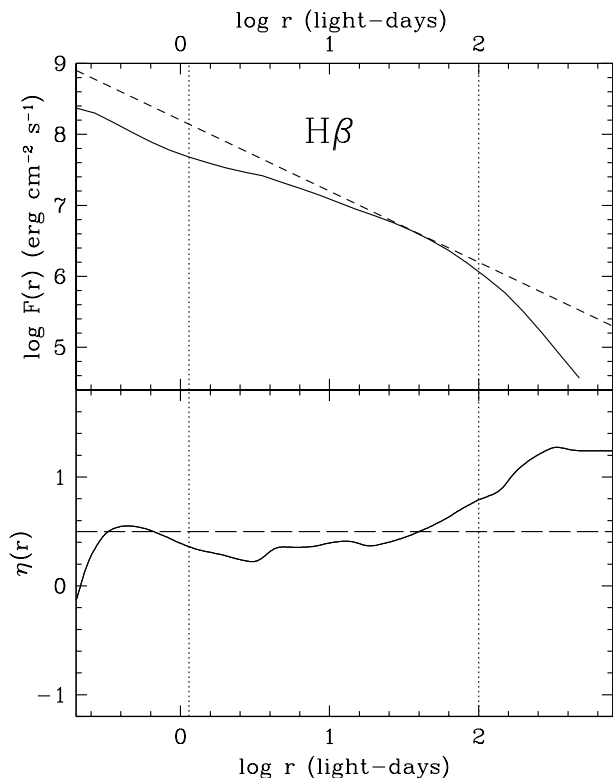


**Figure 1b.** Upper panel – an LOC model prediction of the radial surface emissivity distribution  $F(r)$  for broad  $H\beta$  (solid black line, see text for details). For purposes of comparison, the dashed black line indicates a power-law radial surface emissivity distribution  $F(r) \propto r^\gamma$ , with  $\gamma = -1.0$ , for which  $\eta(r) = -(\gamma/2) = 0.5 \quad \forall r$ . This power-law radial emissivity distribution is tangent to the  $F(r)$  distribution for broad  $H\beta$  at a distance of  $\approx 30$  light-days. Lower panel – the corresponding radial responsivity distributions. The local responsivity for broad  $H\beta$  is smaller than  $\eta(r) = 0.5$  for BLR radii  $< 30$  light-days, and larger than  $\eta(r) = 0.5$  for radii  $> 30$  light-days. The dotted vertical lines indicate the location of the inner and outer boundaries of the fiducial BLR.

malisation, a hydrogen ionizing photon flux  $\log \Phi_H$  (photon  $\text{cm}^{-2} \text{s}^{-1}$ ) = 20.0 corresponds to a continuum source distance of  $R = 15(D_L/77.6 \text{ Mpc})$  light-days. The full grid spans seven decades in gas hydrogen number density  $n_H$  and hydrogen ionizing photon flux  $\Phi_H$ ,  $7 < \log n_H(\text{cm}^{-3}) < 14$ , and  $17 < \log \Phi_H(\text{cm}^{-2} \text{s}^{-1}) < 24$ , stepped in 0.25 decade intervals in each dimension (see e.g. Korista et al. 1997).

Figure 1a indicates the logarithm of the equivalent width (EW) of  $H\beta$  (hereafter  $EW(H\beta)$ ) referenced to the incident continuum flux at  $\lambda 1215\text{\AA}$ , as functions of  $\log n_H$  and  $\log \Phi_H$ . Solid lines represent a decade in EW starting from  $\log(EW) = -1$  at the upper left to  $\log(EW) = 2$  at the lower right. The dotted lines indicate 0.2 dex intervals.

and He II: to  $n=18$ , 15, and 15, respectively. Those levels above were l-averaged. This was done to utilise the improved accuracy of the more sophisticated model atoms appearing in Cloudy version C08. We caution that the default model atoms are unlikely to predict accurate H, He spectra from photoionized gas with physical conditions expected in the BLR.

<sup>3</sup> In this grid of photoionization models, the maximum principal quantum number,  $n$ , with angular momentum resolved levels was increased above its default value in the model atoms of H I, He I,

For reference, the old ‘standard BLR’ parameters (Davidson and Netzer 1979) are marked by the solid star, while the peak EW for this emission line is marked by the solid triangle. The red (dot-dashed) lines indicate the boundaries in  $\log Uc$  (diagonal lines) and  $\log n_H$  (vertical lines) used when calculating the radial surface emissivity distribution for broad H $\beta$  (Figure 1b, upper panel), described below. The upper bound in  $\log Uc \approx 12$  is representative of conditions at which clouds become thermally unstable, and so unlikely to exist stably. We also imagine that the total pressure in the environment depends on the depth within the gravitational potential well of the supermassive black hole, and thus we’ve also set a lower bound in  $\log Uc$ . See Korista and Goad (2000, 2004).

The line EW is a measure of the efficiency by which ionizing continuum photons are converted into emission line photons. The rapid decline in the line EW(H $\beta$ ) near the diagonal line  $\log \Phi_H \approx \log n_H + 10.7$  is due to the hydrogen in the fixed column density slabs becoming fully ionized. Gas near the Compton temperature can be found in the upper left corner of Figure 1a, and the contours of these insignificant EWs are not plotted for clarity. For H $\beta$  as for the other hydrogen and helium optical recombination lines the EW increases with increasing density, a consequence of increasing contributions from collisional excitation (Ferland and Netzer 1979). The general decline in EW(H $\beta$ ) in the direction of increasing incident ionizing photon flux for  $\log \Phi_H$  (photons  $s^{-1} cm^{-2}$ )  $> 18$  is a consequence of increasing line optical depth in this direction, and then eventually increasing photoionizations from excited states. This steady decline in EW(H $\beta$ ) with increasing incident ionizing photon fluxes, noted above, indicates clouds with responsivities  $\eta < 1$  (see equation 2), for this emission line. Where the EW contours are sparse or well-separated with respect to changes in the incident ionizing photon flux, the line EW  $\approx constant$ , and thus these clouds have responsivities  $\eta \approx 1$ . Increasing values in EW with respect to increasing values in incident ionizing photon flux indicate clouds with responsivities  $\eta > 1$ . This is predicted in H $\beta$  at only the smallest incident ionizing continuum fluxes (see Figure 1a).

Average radial surface emissivity distributions for individual lines are generated by summing over the gas density distribution ( $8 < \log n_H (cm^{-3}) < 12$ ) and  $\log Uc = \log \Phi_H - \log n_H$ , as described in Korista and Goad (2000). We use the standard LOC gas density distribution weighting function  $g(n_H) \propto n_H^{-1}$  described in Korista and Goad (2000; see also Baldwin et al. 1995; Bottorff et al. 2002), and which roughly matches the gas density distribution of fragmenting BLR clouds resulting from magnetohydrodynamic instabilities (Krause et al. 2012). The chosen ranges in  $\log n_H$ ,  $\log Uc$ , as indicated by the red dashed-lines in Figure 1a, are nearly identical to those adopted in Korista and Goad (2000, 2001, 2004). In order to investigate the continuum-driven variability of broad H $\beta$ , we compute the radial surface emissivity distribution with respect to incident photon fluxes well below that required to sublimate robust graphite grains at the incident face of the cloud, and likewise well inside the fiducial inner radius of the BLR. As in previous work, we assume an open geometry. That is, we do not address the effect of cloud–cloud shadowing of the incident continuum photons nor the partially transmitted and diffuse continuum and emission line photons, nor their

interaction with the rest of the cloud population on their passage through the BLR.

The model radial surface emissivity distribution  $F(r)$  for H $\beta$  is shown in Figure 1b (upper panel, solid black line). Also shown is the corresponding radial responsivity distribution (lower panel, solid black line). Over the radial extent of the fiducial BLR geometry (indicated by the vertical dashed lines),  $F(r)$  may be approximated by a broken power-law with slope  $\gamma \approx -0.7$  for  $r < 25$  light-days, breaking to a steeper slope,  $\gamma > -2$  for larger radii. This corresponds to a range in radial responsivity  $\eta(r)$  of  $0.35 < \eta(r) < 1.0$  for this line. The effective responsivity for a particular BLR geometry can be determined using a weighted average of the radially dependent responsivities of individual clouds and will, in the absence of significant geometric dilution and windowing effects, lie somewhere within this range. Significantly, this range in  $\eta(r)$  values is similar to the range in measured responsivity  $0.4 < \eta_{eff} < 1.0$  for this line obtained from an analysis of each of the 13 seasons of monitoring data for NGC 5548 (Goad et al. 2004), though the latter is referenced to the optical continuum and not the UV continuum variations. The dashed lines in Figure 1b represent a power-law radial surface emissivity distribution  $F(r)$ , with power-law index  $\gamma = -1$  (upper panel), which equates to a radial responsivity distribution  $\eta(r) = -(\gamma/2) = 0.5$  (lower panel) and is for comparison purposes only.

## 2.2 The driving continuum light-curve

To model the broad emission-line variations in NGC 5548 we first require an appropriate driving ionizing continuum light-curve. Here we generate what we refer to as a “mock” ionizing continuum light-curve for NGC 5548 using as a template the host-galaxy subtracted variable optical continuum light-curve from the 13+ years of ground-based monitoring of NGC 5548 by the AGN Watch collaboration (Peterson et al. 2002; Peterson et al. 2013). To remove the non-variable host galaxy contribution to the optical continuum, we use the updated value from Bentz et al. 2006, derived from HST images and scaled to the appropriate ground-based aperture, and which is approximately 10% larger ( $3.75$  c.f.  $3.37 \times 10^{-15}$  erg  $cm^{-2} s^{-1} \text{\AA}^{-1}$ ) than that used by Romanishin et al. 1995. We then scale the galaxy subtracted optical continuum according to the best estimate of the measured relationship between the UV continuum and optical continuum variability ( $F_{\lambda 5100} \propto F_{\lambda 1350}^\beta$ ), with  $\beta = 0.84 \pm 0.05$  (Bentz et al. 2007) thereby generating a proxy for the driving ionizing continuum light-curve for this source<sup>4</sup>. While modifying the optical continuum in this way provides a reasonable approximation to the amplitude of the UV and so presumably the ionizing continuum variations, it does not

<sup>4</sup> Upon completion of this work we discovered that the quoted value of  $\beta$  had not been corrected for extinction within our Galaxy (Bentz 2014, private communication). The de-reddened value of  $\beta \approx 0.75$  results in a 20% increase in the continuum fluctuation amplitude. Significantly, when combined with the measured relation between H $\beta$  delay and optical continuum luminosity  $\tau(H\beta) \propto L_{opt}^{0.66 \pm 0.13}$ , the size–luminosity relation becomes  $\tau_{BLR} \propto L_{UV}^{0.495}$  in line with photoionization model predictions. We note that this does not substantially alter the findings presented in this work.

reflect the true characteristic timescale of the UV continuum, since the optical continuum is generated at larger and over a broader range in disc radii than the UV continuum. As the designated driver, this continuum is by definition at zero delay with respect to longer wavelength continuum variations and broad emission-line variations. Additionally, as reported in Korista and Goad (2001), the optical continuum is contaminated by a more slowly varying diffuse continuum component arising from BLR clouds and which may represent as much as 20% of the optical continuum flux at 5100Å for NGC 5548. Finally, the limited studies available for the EUV continuum in this source suggests that the variable ionizing EUV continuum displays even larger amplitude variability (Marshall et al. 1997; Chiang et al. 2000) than that used here.

This light-curve is then re-sampled onto a regular 1-day grid by interpolating between bracketing points with uncertainties estimated using a structure function analysis (see e.g. Goad, Korista and Knigge 2004; Goad and Korista 2014, paper 1). Using the mock ionizing continuum we drive the fiducial BLR geometry for a single broad emission-line H $\beta$ , allowing us to compare model emission-line variations with the most extensively studied broad emission-line for which the best possible data is available.

### 3 SIMULATIONS

#### 3.1 Reverberation mapping : Forward modelling

Successful forward models of the broad emission-line region must not only match the observed emission-line variations (amplitude and delay) about their mean level, but in addition, *should also satisfy the necessary energy requirements for that line* (Korista and Goad 2000; Kaspi and Netzer 1999; Horne, Korista and Goad 2003). While it is not the intent of this work to model the broad emission lines and their variability in NGC 5548 in detail, we have checked that the fiducial model geometry (integrated out to 100 light days) and LOC model emissivities predict a *sum* in the luminosities of Ly $\alpha$   $\lambda$  1216 Å and C IV  $\lambda$  1549Å that match the average value from the 1993 HST monitoring campaign (Korista et al. 1995; Korista and Goad 2000).

#### 3.2 The importance of F(r) to the emission line response

First, we investigate how differences in the radial surface emissivity distribution impact upon the model emission-line light-curves. We generate emission-line light-curves using power-law radial surface emissivity distributions ( $F(r) \propto r^\gamma$ ), and power-law indices  $\gamma = -2$  and  $\gamma = -1$ , equivalent to radial responsivity distributions of  $\eta(r) = 1.0$  and  $0.5 \forall r$  respectively, and a physically motivated model for the radial surface emissivity distribution for broad H $\beta$  (Figure 1b, upper panel) constructed for an LOC model of the BLR in NGC 5548, and for which  $0.35 < \eta(r) < 1.0$ . These we compare with the observed 13 yr H $\beta$  emission-line light-curve for NGC 5548. For the power-law radial surface emissivity distributions we assume isotropic line emission. For the physically motivated model, we adopt a line radiation pattern that approximates the phases of the moon (e.g. O’Brien,

Goad and Gondhalekar 1994), with the inward fraction equal to 80% of the total (e.g. Ferland et al. 1992; O’Brien, Goad, and Gondhalekar 1994). For a bowl-shaped geometry, differences in the adopted form of the emission-line anisotropy have little effect on the amplitude of the emission-line response (Goad and Korista 2014, their figure 17), and have a similarly small effect on the emission-line delays, for the range in line-of-sight inclination expected for type 1 AGN.

Model emission-line light-curves are generated by driving the fiducial BLR model with our mock ionizing continuum, assuming a fully non-linear response in the line<sup>5</sup> for a BLR with fixed inner and outer boundaries.

The results of this study are shown in Figure 2. The mock driving ionizing continuum light-curve (black points) and the narrow emission-line subtracted broad H $\beta$  light-curve (red points) as determined using the latest values for the variable narrow emission-line contribution in this source (Peterson et al. 2013) are shown in panel (i). Here and elsewhere, the continuum and emission-line light-curves have been plotted after first normalising to their respective mean values, as calculated from epoch 100 onwards<sup>6</sup>. This is sufficient to allow the whole of the fiducial BLR to respond. For the fiducial bowl-shaped model, the maximum delay at the outer radius of 100 light-days when viewed face-on is only 50 days because gas at larger BLR radii is elevated relative to the mid-plane of a face-on disc and thus lies closer to the observer line of sight (i.e., the bowl has a radially dependent scale height, see equation 3). When viewed at an inclination of 30 degrees, the maximum delay at the outer radius increases to 100 days (see also Figures 1, 4 of Goad, Korista and Ruff (2012)). In order to make a quantitative comparison, we first add noise to each of the model emission-line light-curves, by adding a random Gaussian deviate to each point, with dispersion  $\sigma$  equal to 1% of the flux, and assigning an error bar in a similar fashion. We then compute the continuum–emission-line cross-correlation function (hereafter, CCF), from which we measure the peak delay (or lag) and the centroid (equivalent to the luminosity-weighted radius of the BLR). CCFs are constructed using the implementation championed by Gaskell and Peterson (1987), interpolating on both light-curves. The CCF centroid is measured over the range in delays for which the cross-correlation coefficient exceeds a 0.8 of its peak value. In addition, we measure the average emission-line responsivity for the full 13 yr light-curve using the ratio  $d \log F_{\text{line}} / d \log F_{\text{cont}}$  after first correcting for the mean continuum–emission-line delay

<sup>5</sup> In practice, we calculate the local radial surface emissivity distribution  $\eta(r)$  at the current epoch from the steady-state radial surface emissivity curve  $F(r)$  for that line but shifted according to the continuum level at that epoch (i.e.  $\eta(r) = \eta(r, L(t))$ ). The emission-line light-curve is then determined by summing over the radial surface emissivity distributions (at each epoch), scaled according to the radial covering fraction dependence, and with an appropriate correction for the light-crossing time from the continuum source to the line-emitting region.

<sup>6</sup> We could have instead normalised the model emission-line light-curves to their respective steady-state values, and compared these to the observed continuum and emission-line light-curves averaged over the full 13 yr campaign. We have verified that these differences in the normalisation affect the light-curves shown here at less than the few percent level.

## 8 *Mike, Kirk*

(see Goad, Korista and Knigge (2004), for details). The delays and responsivities reported in Table 2 for these and all other observed and simulated light-curves have been measured relative to the mock driving ionizing continuum.



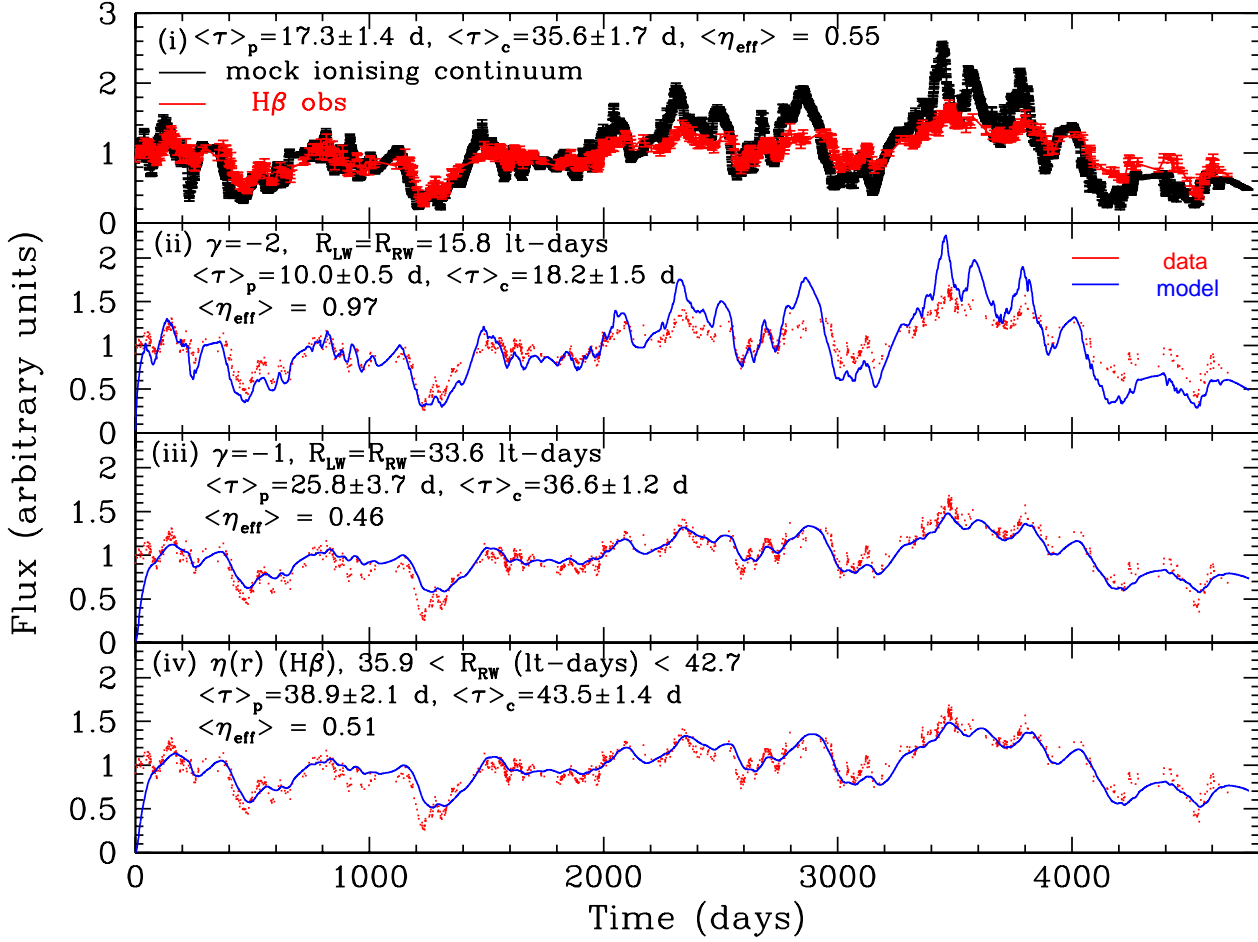


**Figure 2.** Panel (i) – the mock ionizing continuum flux light-curve (black points) and updated narrow-line subtracted broad H $\beta$  flux light-curve (red points). Panels 2 and 3 – the observed broad H $\beta$  flux light-curve (red points) together with model emission-line flux light-curves (solid blue lines) for power-law radial surface emissivity distributions  $F(r) \propto r^\gamma$ , with  $\gamma = -2$ , panel (ii), and  $\gamma = -1$ , panel (iii). Panel (iv) – the observed broad H $\beta$  flux light-curve (red points), together with the model emission-line flux light-curve, assuming a radial surface emissivity distribution from the fiducial LOC model. All light curves have their mean values calculated from day 100 onwards normalised to 1.

Figure 2 panels (i)–(iii) illustrate a number of key points. The measured delay (CCF centroid, lag) and time-averaged responsivity  $\langle \eta_{\text{eff}} \rangle$  for H $\beta$  for the full 13 yr ground-based observing campaign of NGC 5548 *relative to the mock ionizing continuum* are  $35.6 \pm 1.7$  days (CCF centroid), lag  $17.3 \pm 1.4$  days (CCF peak) and  $\langle \eta_{\text{eff}} \rangle = 0.55$  (panel (i)). These values are to be compared with measured delays of  $18.2 \pm 1.5$  days and  $36.6 \pm 1.2$  days (CCF centroid),  $10.0 \pm 0.5$  days and  $25.8 \pm 3.7$  days (CCF Peak) and measured responsivities  $\langle \eta_{\text{eff}} \rangle \approx 0.97$  and  $\approx 0.46$  for light-curves generated using power-law radial surface emissivities with power-law indices  $\gamma = -2$  (panel (ii)) and  $\gamma = -1$  (panel (iii)) respectively.

Power-law radial surface emissivity distributions have by construction  $\eta(r) = \text{constant}$ ; both spatially and temporally, and consequently the responsivity-weighted radius  $R_{\text{RW}}$  is independent of continuum level, i.e., these models cannot breathe. These models also show little evidence for geometric dilution (on average) of the emission line response. That is, the measured time-averaged responsivities  $\langle \eta_{\text{eff}} \rangle = 0.97$  and  $0.46$ , are 97% and 92% of their expected values, while the delays determined from the centroid of the CCF are close in value to the responsivity-weighted radii ( $R_{\text{RW}}$ ). This is to be compared with the significant geometric dilution ( $\approx 20\%$ ) exhibited by the same geometry when viewed face-on (for which geometric dilution is minimised) for the same power-law radial surface emissivity distributions driven by fake continuum light curves with characteristic variability timescale  $T_{\text{char}} = 40$  days (e.g., Figure 14, Goad and Korista 2014, paper 1). We infer from this that the mock ionizing continuum variability light curve we’ve adopted here to drive our models has a  $T_{\text{char}}$  substantially longer than 40 days. Whether this is the case or not in NGC 5548 is unclear, since while the model continuum light curve likely has a more realistic variability amplitude, it remains in essence a time-blurred version of the true driving continuum (§2.2).

The second point of note is that while a steep radial surface emissivity distribution ( $F(r) \propto r^{-2}$ ) is a better match to the observed emission-line variations at the start of the 13 yr campaign (panel (ii), epochs 0–1200), it displays variability over and above that which is observed at later times (e.g., epochs 2000 onwards). We note that even at the start of the campaign, the variability amplitude is too large for this model, and the delay too small on average when compared to the observations, suggesting that the power-law index for  $F(r)$  is flatter than  $-2$ , so that  $\eta(r)$  is in general less than 1. Figure 2 panel (iii) suggests that a shallower radial surface emissivity distribution provides a better match to the observed broad H $\beta$  variations during high continuum states (e.g. epochs 2000–4000), but is generally a poorer match during low-continuum states ( $\approx 400$ –1400). That the observed H $\beta$  emission line behaviour appears to fall between these bounds in responsivity (0.5–1.0) is likely a manifestation of the luminosity-dependent behaviour of the emission line responsivity (Korista and Goad 2004).

We emphasise that no attempt is made to fit the data. Rather, the models we present serve to highlight the observed behaviour of the emission-line light-curves about their respective mean levels, and to illustrate the key physics important in determining not only the emission-line luminosity, but also its response amplitude and delay, for a par-

ticular choice of BLR geometry<sup>7</sup>. Since a steeper radial surface emissivity distribution appears a better match to the observed variability behaviour of broad H $\beta$  at early times, then in the context of our chosen BLR geometry, this suggests that at the start of the campaign the BLR is both more compact (which for a given geometry implies a smaller responsivity-weighted radius, and not necessarily a smaller BLR) and locally has a larger responsivity. Conversely, during the middle and latter parts of the 13 yr campaign, H $\beta$  shows a weaker amplitude response, due to a smaller local emission-line responsivity and increased responsivity-weighted radius. During the latter half of the campaign the continuum level is larger than at the start of the campaign. Thus the response amplitude in H $\beta$  appears to be anticorrelated with continuum level – a behaviour identified in greater detail by Goad, Korista and Knigge (2004), and in qualitative agreement with the predictions of photoionization models (Korista and Goad 2004).

### 3.3 A physical model for $F(r)$

As noted by Korista and Goad (2000, 2004), Goad, Korista and Ruff (2012), and Goad and Korista (2014), the radial surface emissivity distributions of the broad emission lines are in general a poor approximation to a simple powerlaw. This has the important consequence that even for a BLR with static inner and outer boundaries, the BLR may still breathe (e.g. Goad and Korista 2014). In Figure 2 panel (iv), we show the model H $\beta$  emission-line light-curve generated using the radial surface emissivity distribution  $F(r)$  from Figure 1b (upper panel), generated for the fiducial LOC model of NGC 5548. When compared to power-law radial surface emissivity distributions, this model exhibits a number of promising characteristics.

First, the fiducial model’s responsivity averaged over the full 13 yr campaign,  $\langle \eta_{\text{eff}} \rangle = 0.51$  (panel (iv) of Figure 2), is a good approximation to the measured time-averaged value for this line  $\langle \eta_{\text{eff}} \rangle = 0.55$  when referenced to our mock ionizing continuum. Since geometric dilution is small for the adopted driving continuum and BLR geometry (§3.2), then this radial responsivity for broad H $\beta$  determined from a physically motivated model provides a better match to the time-averaged responsivity of this line compared to those predicted by simple power-law description of  $F(r)$  (panels (ii) and (iii) of Figure 2, §3.2)

Second, for a radial surface emissivity distribution  $F(r)$

<sup>7</sup> Currently, dynamical models of the BLR (Pancoast et al. 2012, 2014a,b) do not account for the spatially and time-variable responsivity of the line-emitting gas, assuming instead a constant value for  $\eta(r, t) = 1$  (i.e., a strictly linear response). These models also do not predict the emission line power from the model geometry. It seems unavoidable, however, that the inferred system geometry, emission line luminosity, emission line responsivity and delay are inextricably tied together (and supported by the well known BLR radius–luminosity relation,  $R_{\text{BLR}} \propto L_{\text{UV}}^{1/2}$ ). The present work reinforces the importance of incorporating the physical properties of the line-emitting gas into those forward modelling techniques employed to recover the spatial distribution and kinematics of the line-emitting gas from reverberation mapping data.

that deviates significantly from a simple power-law (Figure 1b, upper panel, solid line versus dashed line), *the responsivity-weighted radius  $R_{RW}$  and measured line responsivity  $\eta_{\text{eff}}$  will vary with continuum level.* Since  $F(r)$  steepens at larger BLR radii (i.e., towards lower ionizing continuum fluxes, Figure 1b, upper panel), the effective responsivity  $\eta_{\text{eff}}$  will increase during low continuum states (Figure 1b, lower panel), due to the larger on average emission-line responsivity and smaller responsivity-weighted radii.

Thus a physically motivated description of the radial surface emissivity distribution for broad  $H\beta$  produces a BLR model which not only breathes, but does so in the correct sense: in low continuum states the BLR responds on shorter timescales and with larger amplitude than in high continuum states, as is observed (Goad, Korista and Knigge 2004). However, while the responsivity weighted radius correlates with continuum flux, its range is rather modest  $35.9 < R_{RW}$  (light-days)  $< 42.7$ . Similarly, if we divide the continuum and emission-line light-curves shown in panel (iv) into contiguous segments, each spanning  $\approx 1000$  days,  $\eta_{\text{eff}}$  is found to vary from  $0.47 < \eta_{\text{eff}} < 0.75$  and importantly anti-correlates with continuum level. Both behaviours are clear signatures of breathing (see Gilbert and Peterson 2003; Goad, Korista and Knigge 2004; Cackett and Horne 2006; Kilerci Eser et al. 2015).

However, the fiducial LOC model does not match the deep excursions exhibited by broad  $H\beta$  during low continuum states (e.g. epochs 1200, 4200), nor in detail the short timescale variations. This largely arises because the fiducial BLR is too large, with a measured delay of  $43.5 \pm 1.4$  d (CCF centroid),  $38.9 \pm 2.1$  d (CCF peak),  $\approx 20\%$  larger (CCF centroid) than that measured for the 13 yr campaign when referenced to our mock driving ionizing continuum. Thus while this model BLR can breathe, and provides a reasonable match to the observed emission-line variations during high continuum states (e.g. epochs 1500–4000), it is still too large on average and responds too weakly during low-continuum states, i.e., within the confines of the BLR boundaries, the adjustments in the local radial surface emissivity in response to continuum variations are not large enough to significantly modify the mean response timescale and amplitude of response in the line. Additionally, the fiducial LOC model and BLR geometry predicts a mean luminosity  $\log L(H\beta)$  ( $\text{erg s}^{-1}$ ) = 41.497,  $\approx$  a factor 2 smaller than the measured 13 yr time-averaged, narrow-line subtracted luminosity for broad  $H\beta$ , once corrected for Milky Way extinction,  $\log L(H\beta)$  ( $\text{erg s}^{-1}$ ) = 41.756 (see Table 1).

In paper I we showed that the measured emission-line response amplitude and delay, for a particular choice of geometry, depend upon (i) the local responsivity in the line-emitting gas, (ii) the monitoring campaign duration and (less so) sampling rate, and (iii) the amplitude and characteristic timescale  $T_{\text{char}}$  of the driving ionizing continuum relative to the maximum delay  $\tau_{\text{max}}$  at the BLR outer radius for a range of plausible geometries given observer line of sight orientation. In the next section we explore the connections between the emission-line luminosity, responsivity, and delay to continuum variations, as well as effects which alter these key quantities without altering the underlying BLR geometry.

#### 4 THE LINK BETWEEN EMISSION-LINE LUMINOSITY, CHARACTERISTIC SIZE AND RESPONSIVITY

For an assumed BLR geometry, the emission-line luminosity is determined by integrating over the radial surface emissivity distribution  $F(r)$ , weighted according to the BLR cloud distribution and covering fraction. Differences in  $F(r)$  for the same geometry will alter: the integrated emission-line luminosity (the energy of the system), the measured continuum–emission-line delays, and the effective emission-line responsivity. For example, if we consider the power-law radial surface emissivity distributions, illustrated in Figure 2, panels (ii) and (iii), a steeper  $F(r)$  (i.e.  $\gamma$  more negative) results in a smaller emission-line luminosity (assuming that  $F(r)$  is normalised to the same value at the BLR inner radius), smaller delays and characteristic sizes, and a larger responsivity. Thus, these quantities can not be treated in isolation but are instead inextricably tied together. Indeed all of these quantities are contained within the continuum–emission-line transfer function  $\Psi(\tau)$  (Blandford and McKee 1982), the function which maps the continuum light-curve on to the integrated emission-line light-curve.

We note that the transfer function  $\Psi(\tau)$  and the response function  $\Psi'(\tau)$  have often been used interchangeably in the literature and as a consequence have been a source of much confusion. However, they are not the same. Here we distinguish between the emission-line transfer function  $\Psi(\tau)$ , which contains the total light from the BLR, and the emission-line response function  $\Psi'(\tau)$ , which deals with only the variable part of the line emission. The latter is recovered from a linearised version of the transfer equation, where constant (or slowly varying) components from both the line and continuum are confined to the background; i.e.  $\Psi'(\tau)$  represents the partial derivative of the line with respect to continuum variations. Weakly responding gas present in the BLR will contribute to the total light in a particular emission line, but less so to its variable light, and so may not be recovered in the response function. Using this distinction, transfer functions and response functions will generally not look the same (they do have the same shape for a powerlaw emissivity distribution because in this case the line responsivity is constant everywhere).

While a different geometrical configuration for the BLR gas could act to enhance the emission-line responsivity, by reducing the delays and thereby increasing the coherence of the emission-line response, *in the absence of geometric dilution, it is the line responsivity that determines the amplitude of the emission-line response to continuum variations.* Furthermore, one cannot simply change the geometry, without affecting: (i) the measured continuum–emission-line delays, (ii) the amplitude of the emission-line response (the responsivity) and (iii) importantly the luminosity for a particular line. Attention to the geometry has mostly focused on the emission-line delays (or lags), yet all three are intimately connected.

We illustrate these connections with two examples. First, reducing the BLR outer boundary incurs a significant penalty in terms of the total emitted power of a particular line, due to the significant loss in surface area which would otherwise be available at large BLR radii (e.g. compare the fiducial model in Table 1 with the truncated model

in which  $R_{\text{out}}$  is set to 50 light-days). This statement holds for any BLR geometry in which the covering fraction dependence is not a steep function of radius. This is especially relevant to the hydrogen recombination lines, which tend to be more emissive as well as more responsive at large BLR radii. Thus to accommodate a smaller BLR outer boundary, a means must be found for boosting the line emissivity and responsivity at smaller radii, such that the energy requirements for a particular line are also satisfied. Secondly, we could also reduce the discrepancy in the fiducial models predicted luminosity by allowing for a larger BLR outer boundary. However, this would come at the expense of still longer continuum–emission-line delays. Attempts to recover the broad emission-line geometry and kinematics which do not account for the power in the continuum and lines should be treated with caution.

#### 4.1 Parameters governing physical conditions that affect $H\beta$ luminosity, characteristic size, and responsivity

Here we explore those effects which act to alter the  $H\beta$  radial surface emissivity distribution  $F(r)$ , and thereby the local responsivity  $\eta(r)$ , and which for an assumed BLR geometry, result in differences in the emission-line luminosity  $L$ , mean response timescale  $\langle \tau \rangle$  and time-averaged responsivity  $\langle \eta_{\text{eff}} \rangle$ . These include: differences in the range in (i) hydrogen gas density, and (ii) hydrogen column density, (iii) allowing for extra-thermal line widths, and (iv) differences in the ionizing continuum normalisation. For expediency, we use photoionization grids previously constructed with this wide range in parameters using Cloudy C90.04 (Ferland et al. 1998), again normalised to match the ionizing continuum luminosity of NGC 5548. While these grids have been constructed using an earlier version of Cloudy than in Figures 1a, b, here we are primarily interested in how changes in key model assumptions affect the luminosity, delay and emission-line responsivity, factors which are intimately connected to the emission-line transfer function.<sup>8</sup>

We show in Figure 3a the  $\text{EW}(H\beta)$  (relative to the incident continuum flux at  $1215\text{\AA}$ ) as a function of  $n_{\text{H}}$ ,  $\Phi_{\text{H}}$  for three choices of cloud hydrogen column density  $N_{\text{H}}$ , as well as for the default cloud column density  $\log N_{\text{H}} (\text{cm}^{-2}) = 23$  with the addition of a significant micro-turbulent velocity for all clouds in the grid. Contours and symbols are as for Figure 1a. In each panel we show the nominal boundaries in parameters contributing to the emissivity functions  $F(r)$  that appear in Figure 3b (see discussion in §2.1).

<sup>8</sup> The SED used for the C90.04 grids is described in Korista and Goad (2000, 2004), and is significantly harder than the Matthews and Ferland (1987) generic quasar continuum adopted for the C08 model grids, with a mean ionizing photon energy which is a factor of three larger. It is for this reason that the diagonal “cliff” in EW, representing the  $\log N(H) = 23$  clouds becoming fully ionized, is shifted by about  $-0.5$  dex in  $\log Uc$  in Figure 3a (upper panel) compared to Figure 1a. However, we note that the Balmer emission lines are not particularly sensitive to the details of the ionizing continuum shape.

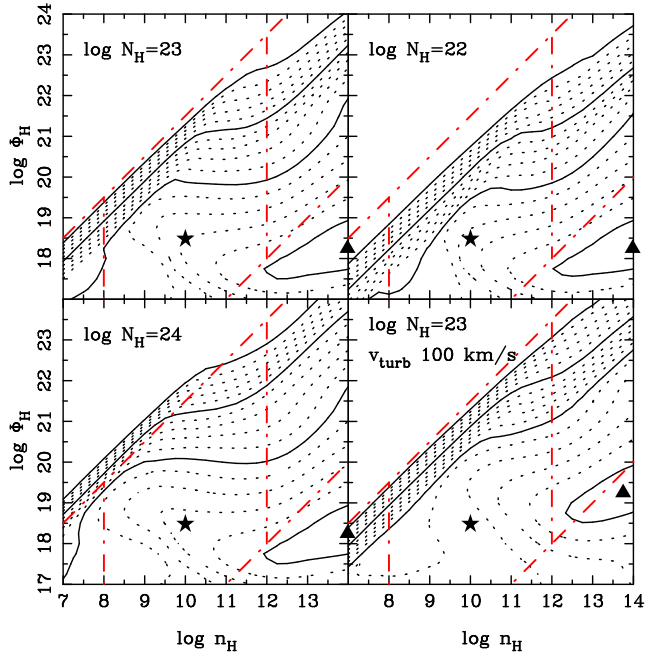


**Figure 3a.** As for Figure 1a, contours of  $\log(\text{EW})$  for broad  $H\beta$  referenced to the incident ionizing continuum at  $1215\text{\AA}$  for full source coverage, as a function gas hydrogen density  $n_{\text{H}}$  and flux of hydrogen-ionizing photons  $\Phi_{\text{H}}$ . The smallest contour corresponds to  $0.1\text{\AA}$  each solid line represents 1 decade, and dotted lines represent 0.2 dex intervals. The solid star marks the old “standard BLR” parameters, the solid triangle the peak EW. Model grids have been computed here using Cloudy version C90.04. Individual panels show the effect on the line EW of changing the adopted column density  $N_{\text{H}}$  from  $\log N_{\text{H}} (\text{cm}^{-2}) = 23$  upper left, to  $\log N_{\text{H}} (\text{cm}^{-2}) = 22$ , upper right, and  $\log N_{\text{H}} (\text{cm}^{-2}) = 24$  (lower left) (see text for details). The lower right panel indicates the effect of introducing extra-thermal line widths, here in the form of a micro-turbulent velocity component  $v_{\text{turb}} = 100 \text{ km s}^{-1}$ , for a fixed hydrogen column density  $\log N_{\text{H}} (\text{cm}^{-2}) = 23$ .

##### 4.1.1 Gas hydrogen number density $n_{\text{H}}$

The radial surface emissivity distribution  $F(r)$  is found to be marginally sensitive to our choice of upper bounds for the distribution function in the hydrogen gas number density,  $n_{\text{H}}$ . Figure 3b, panel (i), illustrates the effect of extending the upper bound in  $n_{\text{H}}$  ( $n_{\text{H}}(\text{max})$ ) from  $10^{12} \text{ cm}^{-3}$  (solid black line) to  $10^{13} \text{ cm}^{-3}$  (dashed red line). For a fixed value in  $\log \Phi_{\text{H}}$ , increasing  $n_{\text{H}}$  increases the  $H\beta$  emissivity due to increased contributions from collisional excitation. Increased  $n_{\text{H}}$  results in enhanced emission over the full radial extent of the fiducial BLR (Figures 3b(i) left panel) and is particularly effective at enhancing the emission measure at smaller BLR radii. When integrated over our fiducial BLR geometry, the net result is a  $\approx 20\%$  increase in the  $H\beta$  luminosity, a marginally smaller responsivity-weighted radius, and locally an enhanced emission-line responsivity (Figure 3b(i), right-hand panel - dashed red line, and Table 1). The enhanced responsivity arises due to the small increase in slope of the radial surface emissivity distribution for BLR radii less than  $\approx 25$  light-days that contains higher density gas with greater efficiency in converting ionizing photons into Balmer emission line photons.

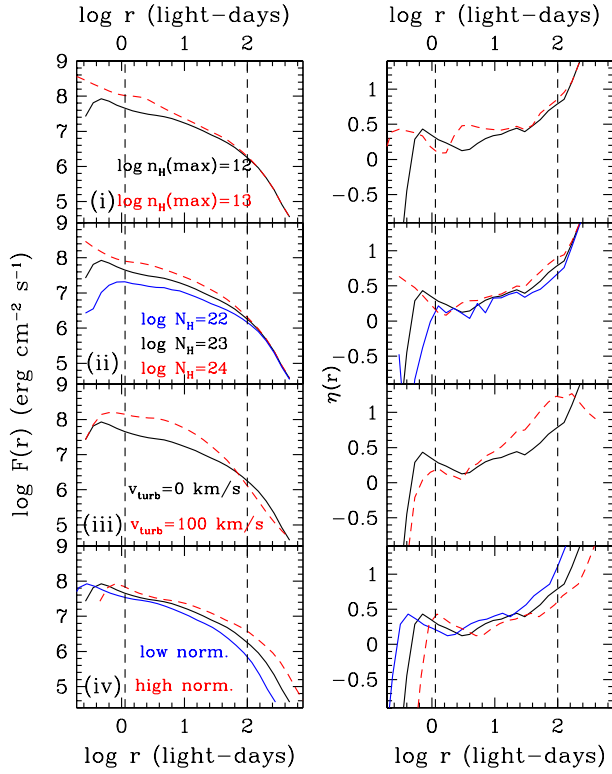


**Figure 3b.** Left panels – Radial surface emissivity distributions for broad  $H\beta$  for an LOC model of NGC 5548. Individual panels show the effect of (i) changing the range in gas hydrogen densities  $n_H$  from  $8 < \log n_H \text{ (cm}^{-3}\text{)} < 12$  (black line) to  $8 < \log n_H \text{ (cm}^{-3}\text{)} < 13$  (dashed red line), (ii) changing the cloud hydrogen column density  $N_H$  from  $\log N_H \text{ (cm}^{-2}\text{)} = 23$  (black line) to 22 (blue line) and 24 (red dashed line), (iii) increasing the micro-turbulent velocity  $v_{\text{turb}}$  from  $0 \text{ km s}^{-1}$  (black line) to  $100 \text{ km s}^{-1}$  (dashed red-line), and (iv) changing the ionizing continuum normalisation by a factor 8.2 from a low (solid blue line) to high (dashed red line) (see text for details). Right-hand panels – the corresponding radial responsivity distributions  $\eta(r)$ .

**Table 1.** The link between emission-line luminosity, characteristic size and responsivity in the steady state.

| H $\beta$  | Cloudy version C08       |                                 |                                 |                           |
|--|--------------------------|---------------------------------|---------------------------------|---------------------------|
|  | log $L$<br>erg s $^{-1}$ | $R_{\text{LW}}$<br>(light-days) | $R_{\text{RW}}$<br>(light-days) | $\eta(r = R_{\text{RW}})$ |
| log $N_{\text{H}}$ (cm $^{-2}$ )= 23<br>(the fiducial model) | 41.497                   | 36.5                            | 41.0                            | 0.55                      |
| $R_{\text{out}} = 50$ light-days                             | 41.235                   | 23.6                            | 25.3                            | 0.42                      |
| log $\Phi_{\text{H}} = 20$ at $R = 7.5$ light-days           | 40.895                   | 18.0                            | 20.2                            | 0.56                      |
| low continuum normalisation                                  | 41.220                   | 33.5                            | 38.6                            | 0.68                      |
| high continuum normalisation                                 | 41.729                   | 38.5                            | 41.6                            | 0.42                      |
| H $\beta$  | Cloudy version C90.04    |                                 |                                 |                           |
|  | log $L$<br>erg s $^{-1}$ | $R_{\text{LW}}$<br>(light-days) | $R_{\text{RW}}$<br>(light-days) | $\eta(r = R_{\text{RW}})$ |
| log $N_{\text{H}}(\text{max})$ (cm $^{-2}$ )= 23             | 41.540                   | 37.2                            | 41.8                            | 0.49                      |
| log $n_{\text{H}}(\text{max})$ (cm $^{-3}$ )= 13             | 41.623                   | 35.6                            | 39.8                            | 0.49                      |
| $v_{\text{turb}} = 100$ km s $^{-1}$                         | 41.768                   | 29.2                            | 35.1                            | 0.82                      |
| log $N_{\text{H}}$ (cm $^{-2}$ )= 22                         | 41.374                   | 39.0                            | 43.0                            | 0.42                      |
| log $N_{\text{H}}$ (cm $^{-2}$ )= 24                         | 41.686                   | 35.0                            | 40.0                            | 0.60                      |

For our adopted luminosity distance  $D_{\text{L}} = 77.6$  Mpc for NGC 5548, the mean narrow-line subtracted H( $\beta$ ) luminosity, corrected for Milky Way extinction ( $A_v = 0.055$ , Schlafly and Finkbeiner 2011) over the duration of the 13 yr ground-based monitoring campaign,  $\log L(\text{H}\beta)$  (erg s $^{-1}$ ) = 41.756. Unless otherwise stated, the continuum has been normalised so that  $\log \Phi_{\text{H}}$  (photons cm $^{-2}$  s $^{-1}$ ) = 20 at a BLR radius  $R = 15$  light-days.

#### 4.1.2 Cloud hydrogen column density $N_{\text{H}}$

The BLR is likely comprised of clouds with a mix of hydrogen column densities. Here we consider the effect of a range in gas hydrogen column density on the line EW as a function of  $\Phi_{\text{H}}$ ,  $n_{\text{H}}$ , for photoionization model grids with fixed total hydrogen column density  $N_{\text{H}}$ . The most obvious effect of increased cloud column density (Figure 3a, panels (i)–(iii)), is a general increase in the EW( $\text{H}\beta$ ) for clouds of larger ionization parameters as the cloud column density increases. The steep decline in EW( $\text{H}\beta$ ) running approximately diagonally across the hydrogen number density-ionizing photon flux plane occurs as the cloud becomes fully ionized in hydrogen.

In Figure 3b, panel (ii), we illustrate radial surface emissivities  $F(r)$  for 3 hydrogen column densities  $N_{\text{H}}$  spanning the range appropriate for BLR clouds  $22.0 < \log N_{\text{H}} (\text{cm}^{-2}) < 24.0$ . With all else equal, the lower column density (solid blue line) leads to smaller values for the radial surface emissivity, reducing the luminosity by a factor  $\approx 1.5$ , and increasing the responsivity-weighted radius by  $\approx 1$  light-day. As can be seen in comparing the upper two panels of Figure 3a, *all else being equal* there are relatively fewer lower column density clouds emitting efficiently in  $\text{H}\beta$  – especially for larger values in  $U = \Phi_{\text{H}}/n_{\text{H}}c$  – and so especially at smaller radii. This results in a flatter radial surface emissivity distribution for clouds of lower column density and consequently smaller responsivity, and a larger responsivity-weighted radius (Table 1). The converse is true for clouds with larger column densities (compare the upper and lower left panels). For  $\log N_{\text{H}} (\text{cm}^{-2}) = 24$ , the luminosity is a factor  $\approx 1.4$  larger, the responsivity  $\approx 20\%$  larger, and with a  $\approx 5\%$  drop in the responsivity weighted radius (see Table 1).

#### 4.1.3 Extra-thermal line widths

As pointed out in paper I, and in Korista and Goad (2004),  $\eta(r)$  can be significantly enhanced by allowing for extra-thermal line widths within the BLR gas. These may be caused by, for example, micro-turbulent velocities (Bottorff et al. 2002), velocity shears, or significant electron scattering within the line emitting gas. The resulting reduction in the central line optical depths increases the line escape probabilities and results in enhanced emission, particularly in lines from clouds that have large central optical depth for local line widths dominated by thermal motions. For the hydrogen recombination lines, these are typically clouds with higher values in the incident ionizing photon flux, and so smaller distances from the central ionizing source. Note that the peak EW has moved upward by  $\approx 1$  dex in  $\Phi_{\text{H}}$ . Micro-turbulent velocities tend to open out the EW contours on the  $\Phi_{\text{H}}$ ,  $n_{\text{H}}$  plane, so that EW contours which formerly were almost constant with  $\Phi_{\text{H}}$ , now tend to follow lines of nearly constant values of  $Uc$ , a diagonal line in the  $\Phi_{\text{H}}$ ,  $n_{\text{H}}$  plane (e.g. notice the differences between the  $10\text{\AA}$  contours shown in Figure 3a, panels (i) and (iv)).

The effect on  $\text{H}\beta$ 's radial surface emissivity  $F(r)$  of increasing the micro-turbulent velocity within the gas cloud from  $0 \text{ km s}^{-1}$  (solid black line) to  $100 \text{ km s}^{-1}$  (dashed red line) is shown in Figure 3b, panel (iii). As above, a significant micro-turbulent velocity boosts the emission across the entire fiducial BLR geometry, but particularly at smaller

BLR radii where the clouds are optically thick in the hydrogen lines. Additionally, when extra-thermal line widths are included, the line responsivity is significantly larger for radii beyond approximately 10 light-days out to the outer boundary. For the fiducial BLR geometry, micro-turbulence results in a significant (factor  $\approx 1.7$ ) increase in the emission-line luminosity, reduces the responsivity-weighted radius by  $\approx 15\%$ , and increases the line responsivity by  $\approx 65\%$  (see Table 1). We note that while this effect results in a better match to the observed  $L(\text{H}\beta)$ , the reduction in  $R_{\text{RW}}$  is smaller than required by the data, and the time-averaged responsivity  $< \eta_{\text{eff}} >$  is too large.

## 4.2 Continuum normalisation

The line emissivity and responsivity distributions within the BLR are sensitive to small changes in the adopted continuum normalisation. Here we distinguish between two types of continuum normalisation. The first relates to uncertainties in the incident ionizing photon flux at a specified radial distance for a BLR of fixed spatial extent. The ionizing photon flux is normally estimated by assuming a continuum SED which is then scaled by the observed continuum flux at a measurable wavelength, for example  $1350\text{\AA}$  or  $5100\text{\AA}$  (rest frame), for an assumed luminosity distance and after applying corrections for extinction within the Milky Way galaxy and potentially also the host galaxy. Since  $\Delta \log r = -0.5 \times \Delta \log \Phi_{\text{H}}$  for a given ionizing luminosity and SED, small uncertainties in the continuum normalisation in this case will shift  $F(r)$  towards the left (for lower continuum normalisations) or towards the right (for higher continuum normalisations), within the confines of the BLR (see e.g. Figure 3b panel (iv), solid blue and red-dashed lines, respectively). These differences will lead to changes in line  $L$ ,  $R_{\text{RW}}$  and  $\eta(r = \text{RW})$  (Korista and Goad 2004; Goad and Korista 2014). To illustrate this point low and high continuum normalisations corresponding to a factor  $\approx 8$  range in ionizing continuum flux (e.g. Figure 3b, lower left panel), increases  $L(\text{H}\beta)$  by a factor  $\approx 3$ , increases  $R_{\text{RW}}$  from 38.6–41.6 light-days, and decreases  $\eta(r = \text{RW})$  from 0.68–0.42 (see Table 1). Figure 4 panel (ii) illustrates model broad  $\text{H}\beta$  light-curves for low (solid green line) and high (solid black line) continuum normalisations corresponding to the same factor of  $\sim 8$  range in the ionizing continuum normalisation (see Table 2 for details). In all cases the inner and outer boundaries,  $R_{\text{in}}$  and  $R_{\text{out}}$ , have been kept fixed at their starting values. For a BLR with static boundaries a lower continuum normalisation appears to be favoured.

The continuum normalisation is also determined by the way in which the incident ionizing photon flux  $\Phi_{\text{H}}$  maps to BLR radial distance  $r$ . An example of this, is a particular choice of source luminosity distance  $D_{\text{L}}$ . Uncertainties in  $D_{\text{L}}$  will alter the radial surface emissivity distribution and the radial scale, but in a self-similar way, i.e.,  $R_{\text{out}}/R_{\text{in}}$  remains invariant. This is equivalent to a reassignment of the radial scale in Figure 1b. Thus while the continuum and emission line luminosities along with the BLR size (lag) will change, the radial dependence of the surface emissivity and responsivity distributions within the confines of the BLR will not. For lower continuum normalisations of this second type, the BLR will be smaller, with a corresponding drop in the emission-line luminosity (though the emission line EW

remains the same). We note here that though the BLR is now more compact,  $R_{\text{out}}$  remains equal to  $R_{\text{subl}}$ . However, the emission line response amplitude will be unchanged if the effects of geometric dilution are weak.

In Figure 4 panel (iii) we illustrate this effect by reducing the mapping of  $r$  onto  $\Phi_{\text{H}}$  by a factor 2, resulting in a factor 4 drop in the mean emission-line luminosity (see Table 1)<sup>9</sup>. Since differences in the chosen value of  $D_{\text{L}}$  alter the luminosities of both line and continuum alike, the discrepancy between the measured and model emission line luminosities (factor  $\approx 2$  for  $\text{H}\beta$ ) will remain the same. The net effect is thus a decrease in the responsivity-weighted radius ( $17.7 < R_{\text{RW}}$  (light-days)  $< 21.1$ ), while the predicted time-averaged emission-line responsivity ( $\langle \eta_{\text{eff}} \rangle = 0.53$ ) is similar to the fiducial model (Table 1). Indeed setting aside the discrepancy in the emission line luminosity, Figure 4, panel (iii) indicates that a lower continuum normalisation of this type provides a far better representation of the data in terms of response amplitude and delay.

The fidelity of the reproduction of the majority of the observed features in the  $\text{H}\beta$  emission-line light curve is testament to the validity of using the scaled optical continuum as a proxy for the driving ionizing continuum.

<sup>9</sup> While a large uncertainty in the mapping of the cloud–source distance  $r$  to the incident hydrogen ionizing photon flux  $\Phi_{\text{H}}$  due to an uncertainty in the luminosity distance is unlikely, an effect of this nature may also arise if the ionizing continuum is highly anisotropic (e.g., Netzer 1987; Nemmen and Brotherton 2010) so that the ionizing continuum flux incident on BLR clouds, and that which we infer from the observed continuum flux are not the same. If BLR clouds are located at large polar angles, and we observe them from much smaller ones, then the measured emission line EWs will be artificially reduced if continuum anisotropy is important.



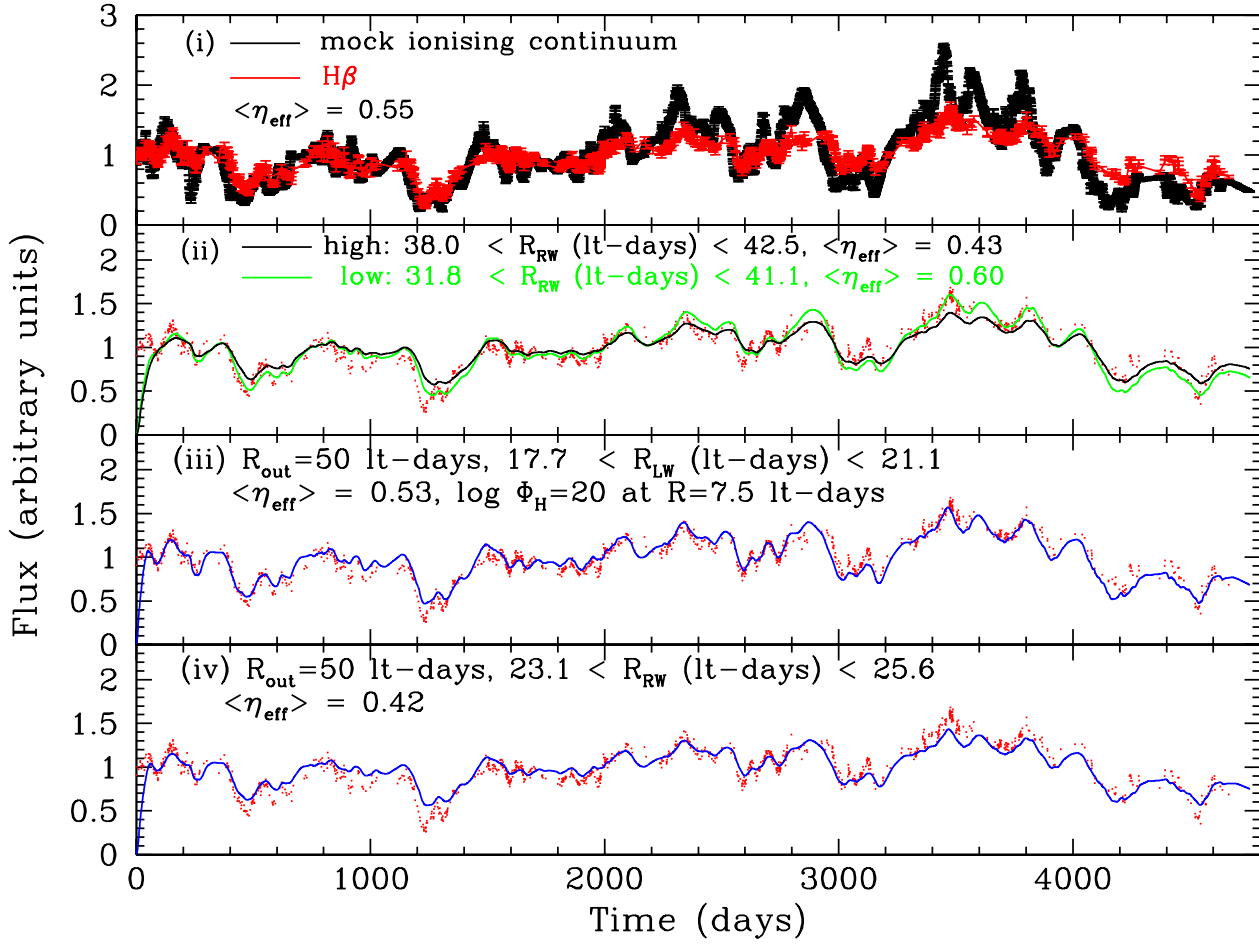


**Figure 4.** Model broad  $\text{H}\beta$  emission-line light curves for our fiducial BLR geometry for (ii) high and low ionizing continuum normalisations (solid black and green lines respectively), (iii) a model BLR with a factor 2 reduction in the luminosity distance, and (iv) the fiducial BLR truncated at an outer radius of 50 light-days (solid blue line). Both (iii) and (iv) result in a smaller BLR and lower line luminosities, but only (iii) results in enhanced amplitude response in the line. The quoted range in  $R_{\text{RW}}$  corresponds to the range in measured CCF centroid for the 13 seasons of data.

### 4.3 Is $R_{\text{out}} \ll R_{\text{subl}}$ ?

We have also considered the possibility that our model BLR is simply too large for our particular continuum normalisation. The mean response timescale for broad H $\beta$  for the fiducial BLR model, determined from the centroid of the 1-d responsivity-weighted response function  $R_{\text{RW}}$ , is  $\approx 41$  light-days. This is  $\approx 20\%$  larger than the average continuum-emission-line delay of  $35 \pm 1.7$  days determined for broad H $\beta$  (using our mock driving ionizing continuum) over the 13 yr ground-based monitoring campaign of NGC 5548. While a smaller outer boundary will act to reduce the responsivity-weighted radius of the BLR, and consequently reduce the possible effect of geometric dilution (Goad and Korista 2014), it has a number of undesirable consequences. First and foremost, the emission-line luminosity is reduced. For the fiducial bowl-shaped BLR, a factor 2 reduction in the BLR outer radius equates to a factor  $\approx 2$  reduction in the emission-line luminosity for broad H $\beta$ . The luminosities of other emission-lines will also be reduced though by differing amounts. Secondly, photoionization model calculations suggest that for most emission lines, gas at larger radii (or equivalently lower ionizing photon fluxes) will have the largest responsivity (see Figure 1, lower panel, for H $\beta$ ). Thus the emission-line responsivity in the absence of geometric dilution, when averaged over the BLR cloud distribution, will tend to decrease if we remove those contributions to the line responsivity arising from gas at large BLR radii. This is especially important for the geometry considered here because as we have already shown (§3.2), there is little geometric dilution. Thus for the fiducial BLR geometry, the variability amplitude of a particular line in response to continuum variations is determined almost exclusively by the emission-line responsivity for that line. *Note that if the local responsivity is small, the amplitude of the variations would be similarly small (for the same driving continuum), regardless of how compact the BLR is.*

Figure 4 panel (iv) illustrates the effect of truncating the outer BLR at a radius of 50 light-days. Removing the high responsivity gas at large BLR radii reduces the emission line luminosity, the emission-line delay and its time-averaged responsivity. Thus when compared to the fiducial model (Figure 2 panel (iv)), the broad emission-line is less luminous (by a factor  $\approx 2$ ), arises from a more compact region ( $23.1 < R_{\text{RW}}$  (light-days)  $< 25.6$ ), and has a smaller amplitude response in the line ( $\langle \eta_{\text{eff}} \rangle = 0.42$  c.f. 0.51). Once again, these results indicate the deep connection between  $L$ ,  $R_{\text{RW}}$  and  $\eta$ .

We next compare this truncated BLR with one of the same size and outer radius, but different radial surface emissivity distributions  $F(r)$  arising from different mappings of  $r$  onto  $\Phi_{\text{H}}$ . When compared with Figure 4 panel (iii), the truncated BLR has a lower amplitude response in the line, because for this line, the more responsive gas which is normally found at lower ionizing photon fluxes (i.e. larger BLR radii) has now been removed.

That the emission-line luminosity, characteristic size and responsivity are intimately connected and cannot be treated in isolation is again evident. Altering the models to address just one of these can adversely effect the others. These connections should provide strong constraints on BLR models, as well as help break the degeneracies inherent in

the interpretation of emission line transfer functions. Consideration of additional emission lines will further strengthen these tensions.

## 5 THE NATURE OF THE BLR INNER AND OUTER BOUNDARIES

The models described thus far have been static, in the sense that the spatial extent of the BLR has remained constant in time. These models can still breathe, because in general the radial surface emissivity distribution within the confines of the BLR inner and outer boundaries is not a simple power-law, and consequently the local responsivity and hence responsivity-weighted radius will vary with continuum level. However, for the fiducial model the BLR is underluminous in H $\beta$  by a factor  $\approx 2$ , and is in general too large, while the *measured range* in responsivity appears too small, and in particular fails to match the observed variations in H $\beta$  during low continuum states. Here, we investigate the possibility that the BLR may in addition adjust its overall spatial extent in response to changes in the ionizing continuum flux.

### 5.1 The BLR inner boundary $R_{\text{in}}$

For the fiducial model the BLR inner boundary  $R_{\text{in}}$  has been set to  $200 R_{\text{g}} \approx 1.14$  light-days for a  $10^8$  solar mass black hole. The location of this boundary was motivated in part by the small measured delay in He II 1640 in NGC 5548 (e.g., Korista et al. 1995), although the precise location of the inner boundary is unknown. However, we note that gas at such small radii has very little surface area, and thus its contribution to the total power of a particular emission line is modest at best. Additionally, at small BLR radii the gas becomes over-ionized and the lines thermalised. Thus, unless the BLR is geometrically thin, then provided that the specified inner boundary is small, relatively large uncertainties in its location may be tolerated. In what follows unless otherwise noted, we let the location of the BLR inner boundary vary with continuum level according to  $R_{\text{in}} \propto C(t)^{1/2}$ . For H $\beta$  and other emission lines that form at large BLR radii, this has almost no effect on the emission line variability.

### 5.2 The BLR outer boundary $R_{\text{out}}$

For the fiducial model the location of the BLR outer boundary  $R_{\text{out}}$  is particularly significant because although the radial surface emissivity distribution steepens as  $r$  increases, (Figure 1b), this fall in surface emissivity is (partially) compensated for by a steady increase in the available surface area. Here we have set  $R_{\text{out}} = 100$  light-days, a distance beyond which the mean continuum flux is low enough that robust dust grains (e.g., graphite) can form and survive. When present ionizing continuum and emission-line photons are destroyed on grains, and consequently (along with the decrease in the gas phase abundances) the line emission can drop significantly (Netzer and Laor 1993).

One consequence of a large surface area at large BLR radii is that small changes in the location of the BLR outer boundary, whether dynamical, or related to ionizing continuum variations, will produce significant variation in the line

emission at large radii. This then leads to significant variation in the emission-line delay and amplitude of response, if gas exists at these radii. *Thus understanding the nature of the BLR outer boundary has become one of the key goals of AGN variability studies.* In what follows we investigate the behaviour of a dust-bounded BLR.

### 5.3 A dust-bounded BLR model

Thus far our model BLR has been described by inner and outer boundaries exterior to which the line emission is assumed to be zero (i.e. a BLR which is truncated at both the inner and outer radius). At small BLR radii this is likely to be a good approximation since: (i) the line emission decreases rapidly at the highest incident ionizing photon fluxes, and (ii) for most geometries, the inner BLR contributes very little to the overall emission (an area effect). However, for the BLR outer boundary this assumption is likely invalid, since the reservoir of gas feeding the BLR likely originates in the dusty torus at still larger radii. Alternatively, a truncated BLR, for which the outer radius lies well within the location of the hot dust, may arise if gas at larger radii is largely shielded from a direct view of the ionizing continuum source.

Here, we assume that the BLR extends all the way to the inner edge of the dusty torus, i.e., the distance to the hot dust. Where grains are able to form and survive, they can compete efficiently for ionizing photons and act to suppress, though not extinguish, the formation of lines. Thus bounding this model BLR there exists a dusty region where the line-reprocessing efficiency is significantly reduced. At sufficiently large incident photon fluxes, grains charge up and heat up and eventually sputter and sublimate. The distance at which grains sublime depends on their chemical composition (e.g., graphites vs. silicates) and size distribution (e.g. Barvainis 1987). Where grains are sufficiently depleted line formation will efficiently cool the gas. Thus the BLR outer boundary could move outwards with increasing continuum source luminosity. Larger grains are more robust than smaller grains. Thus condensation onto grains during lower continuum flux states is most likely to occur onto larger grains. During these low continuum flux states the effective line-emitting boundary of the BLR could move inwards<sup>10</sup>. In the context of a dust-bounded BLR we here refer to an “effective BLR outer boundary”,  $R_{\text{eff}}$ , which represents the point beyond which the line emission is significantly suppressed. The rate at which  $R_{\text{eff}}$  moves in response to continuum variations is governed by two important timescales, the dust condensation and sublimation timescales,  $\tau_{\text{cond}}$  and  $\tau_{\text{subl}}$  respectively.

Here we distinguish between the microscopic dust formation and destruction timescales, which for individual grains is of order minutes–days, and the macroscopic (or

global) dust formation and destruction timescales which is of order months–years for grains largely shielded within or beyond the BLR gas, and relevant to the discussion here (e.g. Kishimoto et al. 2013, 2011; Hönig and Kishimoto 2011). If the macroscopic dust sublimation timescale  $\tau_{\text{subl}}$  is very much longer than the macroscopic dust condensation (formation) timescale  $\tau_{\text{cond}}$ , then the location of the BLR outer boundary will be largely insensitive to high continuum states, but will tend to move inwards on average during low continuum states. Conversely, if the dust condensation timescale is long compared to the dust sublimation timescale, the BLR outer boundary will tend to move outwards during high continuum states and remain there, unless there is a significant period in which the ionizing continuum source remains in a low state.

As viewed from the ionizing continuum source, at a given instant in time, emission line gas located at the same radial distance will be responding to the same ionizing continuum state. Gas located at larger radial distances will be responding to different (prior) continuum states. Thus there will be some regions in which the efficiency of line formation is increasing, while in others it is decreasing, depending on the prior continuum history, bracketed by regions in which the line emission efficiency is not affected by the presence of dust. Furthermore, when viewed by an external distant observer, gas located at the same radial distance will appear to be responding to different ionising continuum states due to differences in the total light-travel time (reverberation). Thus the observed location of  $R_{\text{eff}}$  at a particular instant in time is determined by both the local gas–grain physics and reverberation effects within the spatially extended BLR.  $R_{\text{eff}}$  is therefore better described as a “fuzzy” or “soft” outer boundary.

#### 5.3.1 A time-dependent efficiency factor $\epsilon(r, t)$

In order to implement a dusty BLR outer boundary within the context of our model, we introduce a time-dependent line-emission efficiency factor  $\epsilon(r, t)$  which we use to scale the radial surface emissivity distribution  $F(r)$ , and which in the steady-state takes a value of 1.0 in the absence of dust and a value of 0.1 when dust is present. Initially we set the outer boundary  $R_{\text{out}}$  to be located at the distance to the hot dust  $R_{\text{out}} = 100$  light-days, equivalent to the radius at which the temperature falls below the dust sublimation temperature  $R_{\text{out}} = R_{\text{subl}}$ . Thus in the steady-state  $\epsilon(r, t) = 1.0$  for  $r \leq R_{\text{subl}}$ , and  $\epsilon(r, t) = 0.1$  for  $r > R_{\text{subl}}$ . As the continuum varies, the location of the dust boundary is assumed to scale as  $R_{\text{subl}} \propto C(t)^{1/2}$  (as indicated by the solid red line in the upper panel of Figure 5, 7), similar to the relationship between the distance to the hot dust and source luminosity found among a sample of nearby AGN (Suganuma et al. 2004; 2006)<sup>11</sup>. NB the form of the driving continuum light-curve is similar to that illustrated by the solid red line in the upper panel of Figures 5, 7 and may be reconstructed by

<sup>10</sup> In the fiducial model the BLR gas occupies the surface of an approximately bowl-shaped geometry (§2). The dust we assume to follow the extension of this geometry out to larger radii, starting from a radial distance  $R_{\text{subl}}$ , the distance at which robust grains can form and survive. Note, here that the location of  $R_{\text{subl}}$  is confined to the bowl-surface, and is time-dependent, sliding along the bowl surface in response to variations in the ionizing continuum flux, i.e.  $R_{\text{subl}} = R_{\text{subl}}(C(t))$ .

<sup>11</sup> The relationship between the continuum luminosity and the inferred distance to the hot dust is found to be far shallower in individual sources, possibly as a consequence of long dust condensation and dust sublimation timescales when compared to the characteristic continuum variability timescale  $T_{\text{char}}$ .

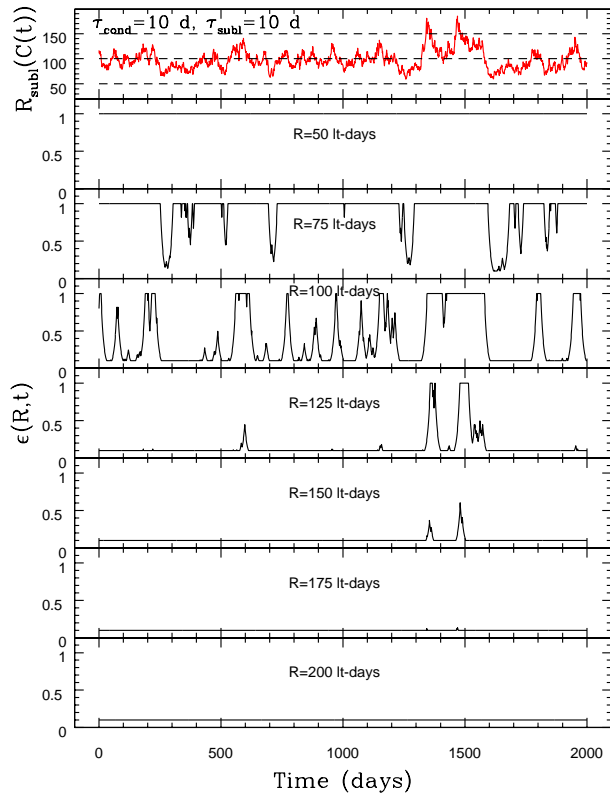


**Figure 5.** Upper panel - the predicted location of  $R_{\text{subl}}$  as a function of time (days) for a dust-bounded BLR in which the location of the dust boundary varies as  $C(t)^{1/2}$ , and for which the local line re-processing efficiency factor  $\epsilon(R, t)$  depends upon the location of  $R_{\text{subl}}$ , and the dust sublimation and dust condensation timescales,  $\tau_{\text{subl}}$  and  $\tau_{\text{cond}}$  respectively. Shown are the results for  $\tau_{\text{subl}} = \tau_{\text{cond}} = 10$  days. Panel 2–8, the re-processing efficiency factor  $\epsilon(R, t)$  as a function of time (days) at fixed BLR radii  $R$ .  $\epsilon(R, t)$  displays rapid falls and sharp rises which appear symmetrical in shape.

normalising this curve to its mean value and squaring the amplitude.

Here, we assume that as the continuum flux rises the line re-processing efficiency factor  $\epsilon(r, t)$  for gas lying interior to the current location of  $R_{\text{subl}}$ , increases exponentially from its current value until it reaches a maximum value 1.0 on a timescale  $\tau_{\text{subl}}$ , where  $\tau_{\text{subl}}$ , the macroscopic dust sublimation timescale, represents the timescale over which grains (embedded within the BLR clouds) are significantly depleted by UV photons. Thus, for a given increase in the continuum flux, clouds which lie interior to the region bounded by  $R_{\text{subl}}$ , will either emit at 100% efficiency, or their efficiency will grow exponentially, according to  $\epsilon(r, t) = \min[\epsilon(r, t-1)e^{1/\tau_{\text{subl}}}, 1.0]$ . Conversely, as the continuum flux decreases, we assume that for gas formerly bounded by  $R_{\text{subl}}$  but now lying exterior to  $R_{\text{subl}}$ , the line re-processing efficiency factor  $\epsilon(r, t)$  decreases exponentially from its current value to a minimum efficiency factor of 0.1, on a characteristic timescale,  $\tau_{\text{cond}}$ , the macroscopic dust condensation timescale, such that  $\epsilon(r, t) = \max[\epsilon(r, t-1)e^{-1/\tau_{\text{cond}}}, 0.1]$ . Thus at any instant in time, there will be a dust-free zone

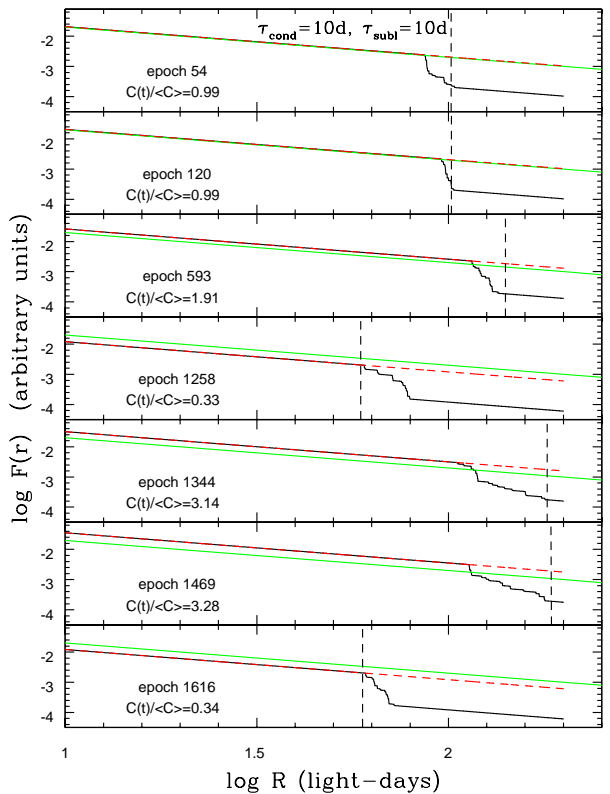


**Figure 6.** Snapshots of the instantaneous radial surface emissivity distribution  $F(r)$  as a function of continuum level  $C(t) / \langle C \rangle <$  (solid black line), for the fiducial bowl-shaped BLR geometry described in section 5.3. Also shown are the steady-state radial surface emissivity distribution (solid green line) together with the expected radial surface emissivity distribution assuming  $\epsilon(R, t) = 1.0$  (dashed red line). The dashed vertical line represents the predicted location of  $R_{\text{subl}}$  for the epoch shown, assuming that the location of  $R_{\text{subl}}$  scales as  $C(t)^{1/2}$ . For this example,  $\tau_{\text{subl}} = \tau_{\text{cond}} = 10$  days. Since the dust sublimation and condensation timescales are equivalent, the location of the soft boundary  $R_{\text{eff}}$ , as indicated by the sharp drop in the radial surface emissivity distribution (solid black line), is well-matched to the predicted location of the dust boundary for the current continuum level (dashed vertical line).

in which the line re-processing efficiency  $\epsilon(r, t) = 1.0, \forall t$ , a dusty zone, in which  $\epsilon(r, t) = 0.1, \forall t$ , bounding an intermediate zone where grains are in the process of either being formed or destroyed, and for which the line re-processing efficiency lies in the range  $0.1 < \epsilon(r, t) < 1.0$ , and is either decreasing exponentially to a minimum of 0.1 on a timescale  $\tau_{\text{cond}}$  due to a decrease in the continuum flux or increasing exponentially to a maximum of 1.0 on a timescale of  $\tau_{\text{subl}}$  for a rising continuum flux. In the limit of  $\tau_{\text{subl}}, \tau_{\text{cond}}$  very small, the location of the effective BLR outer boundary  $R_{\text{eff}}$  varies in lock-step with the ionizing continuum (i.e.  $R_{\text{eff}} \propto C(t)^{1/2}$ ). This we here refer to as a variable hard boundary model. Conversely, for  $\tau_{\text{subl}}, \tau_{\text{cond}}$  very large, the effective BLR outer boundary remains essentially static and behaves in a similar fashion to the fixed boundary LOC model explored in §3. The light-curve generated by this model will resemble that of Figure 2 panel (iv), except

that the model is now computed beyond 100 light-days out to a maximum radius  $R_{\max}$  (here set at 200 light-days) and the line re-processing efficiency  $\epsilon(r, t)$  changes abruptly either side of this boundary (from 1.0 to 0.1). For  $R_{\max} = 200$  light-days the total covering fraction is  $\sim 70\%$  for the fiducial bowl-shaped geometry (c.f. 50% at  $R = 100$  light-days, see Goad, Korista and Ruff 2012, for details).

### 5.3.2 A simple toy model

To illustrate the general behaviour of a dust-bounded BLR and its sensitivity to the dust sublimation and dust condensation timescales, we have generated model emission-line light-curves using a driving continuum light-curve which can be described by a damped random walk<sup>12</sup> in the logarithm of the flux (e.g. Kelly et al. 2009; MacLeod et al. 2010; Goad and Korista 2014, paper 1) and the fiducial BLR model with a power-law radial surface emissivity distribution with slope  $-1$ , bounded by dust at its outer edge. That is, in the steady state  $R_{\text{subl}}(C(t) = \langle C \rangle = 1) = 100$  light-days. We have deliberately chosen a powerlaw radial surface emissivity distribution, since in this case  $\eta(r) = \text{constant} \forall r$ , in the steady-state, and thus breathing can only occur via changes in the location of the BLR boundaries. The radial surface emissivity distribution is computed out to a maximum radius  $R_{\max}$  of 200 light-days, and in the steady-state the line re-processing efficiency factor  $\epsilon(R, t)$  is assumed to be 1.0 for gas lying interior to  $R_{\text{subl}}$ , and 0.1 for gas lying exterior to  $R_{\text{subl}}$ .

We consider two scenarios for a BLR with a dusty outer boundary. For the first, we set the dust sublimation and dust condensation timescale to be equivalent to one another, so that grains are depleted and reform on the same timescale, here  $\tau_{\text{subl}} = \tau_{\text{cond}} = 10$  days. For the second, we set the dust sublimation timescale to be factor ten longer than the dust condensation timescale,  $\tau_{\text{subl}} = 100$  days, and  $\tau_{\text{cond}} = 10$  days, so that while grains are depleted rather slowly, they rapidly reform. For the latter, quoted values of  $\tau_{\text{subl}}$  and  $\tau_{\text{cond}}$  were chosen to suppress large amplitude emission-line variations during high continuum states, while allowing for a more compact BLR with a smaller responsivity-weighted radius, during prolonged low continuum states.

The results of our simulations are shown in Figures 5–8. Each model is bounded at large radii by  $R_{\text{subl}}$  which as for the variable hard boundary model scales as  $C(t)^{1/2}$  (Figure 5, upper panel). However, since the line re-processing efficiency is low for radii  $R_{\text{subl}} < r < R_{\max}$ , the effective outer boundary  $R_{\text{eff}}$ , as indicated by the sharp drop in line emissivity (figure 6, solid black line) at larger radii, is smaller than  $R_{\max}$ . Note that the range in radii over which changes in the re-processing efficiency occur is extensive, spanning  $\sim 60$ –185 light-days, appropriate for the  $\sim$  factor of 9.6 range (max/min) in continuum level.

For the first simulation, we set  $\tau_{\text{subl}} = \tau_{\text{cond}} = 10$  days. Consequently, the temporal behaviour of the re-processing

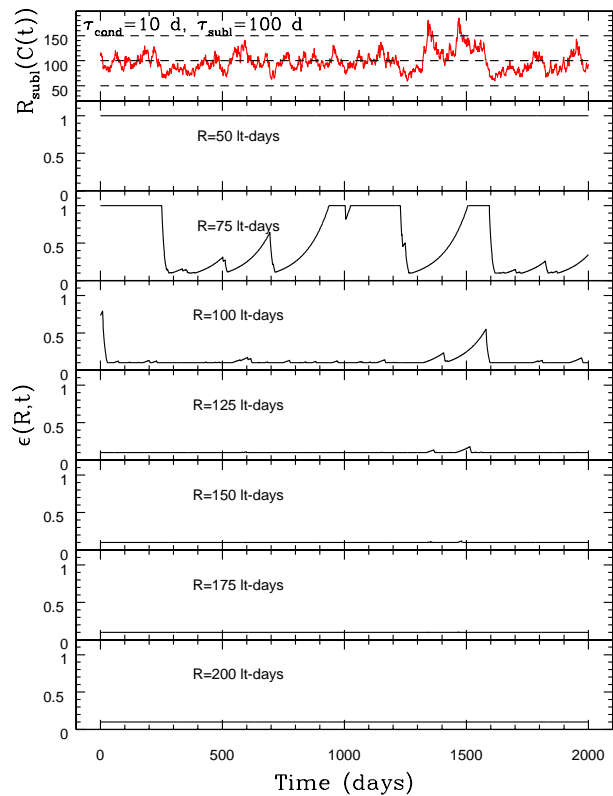


**Figure 7.** Upper panel - the predicted location of  $R_{\text{subl}}$  (solid red line) as a function of time (days) for a dust-bounded BLR with  $\tau_{\text{cond}} = 10$  days and  $\tau_{\text{subl}} = 100$  days. Panels 2–8, the model re-processing efficiency factor  $\epsilon(r, t)$  as a function of time (days), for BLR radii of 50, 75, 100, 125, 150, 175 and 200 light-days respectively. For this model, the time-dependent line re-processing efficiency factor shows rapid declines followed by slow rises.

efficiency  $\epsilon(r, t)$  at fixed radial position  $r$  is characterised by symmetric rises and falls, and by significant excursions in re-processing efficiency on relatively short timescales (Figure 5, panels 2–8). In Figure 6 we show snapshots of the instantaneous radial surface emissivity distribution  $F(r, C(t))$  (solid black line) at seven epochs, chosen to illustrate a broad range in continuum level. Also shown is the steady-state radial surface emissivity distribution (solid green line) together with the radial surface emissivity distribution at the current epoch, assuming  $\epsilon(r, t) = 1.0 \forall r$  (dashed red line). One consequence of adopting similar dust sublimation and dust condensation timescales is that the sharp drop in the radial surface emissivity distribution  $R_{\text{eff}}$  more closely coincides with the predicted location of  $R_{\text{subl}}$  for the concurrent value of the continuum flux (Figure 6, vertical dashed lines).

For the second simulation  $\tau_{\text{subl}}$  is a factor of 10 longer than  $\tau_{\text{cond}}$ . Variations in  $\epsilon(r, t)$ , are here characterised by a rapid decline in the re-processing efficiency during low continuum states followed by a more gradual increase in the re-processing efficiency with increasing continuum level as the dust is eroded (Figure 7). The location of  $R_{\text{eff}}$  therefore decreases significantly on relatively short timescales following a drop in continuum level, but moves outwards only very slowly as the continuum level starts to rise. Thus a

<sup>12</sup> We note that a damped random walk has been found to be a poor match to the broad band variability behaviour of AGN observed by Kepler (Mushotzky et al. 2011), albeit in a small sample of objects and for light-curves which only probe timescales appropriate for the disc light-crossing time.

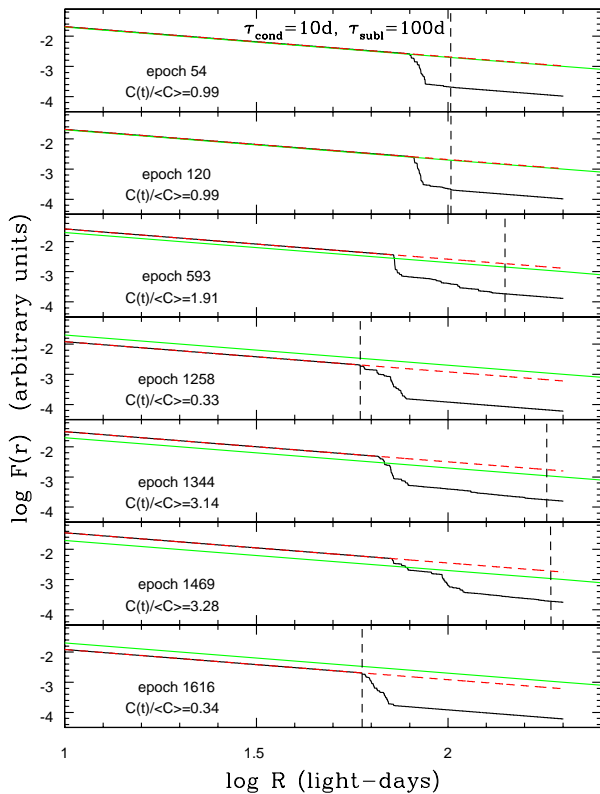


**Figure 8.** As for Figure 6, adopting  $\tau_{\text{cond}} = 10$  days, and  $\tau_{\text{subl}} = 100$  days. A strong hysteresis is evident in the radial surface emissivity distributions such that the location of the soft boundary  $R_{\text{eff}}$  (as indicated by the sharp drop in radial surface emissivity distribution) correlates only poorly with the predicted location of  $R_{\text{subl}}$  (as indicated by the vertical dashed line) for this continuum level.

strong hysteresis in the location of  $R_{\text{eff}}$  is a defining characteristic of models in which there is a strong mismatch between the macroscopic dust sublimation and dust condensation timescales (c.f. the location of the sharp drop in the solid black lines with the dashed vertical lines in Figure 8).

## 6 A DUST-BOUNDED BLR MODEL FOR NGC 5548

We now turn our attention to modelling the broad  $\text{H}\beta$  emission-line light-curve in NGC 5548 assuming a dust bounded BLR with time variable spatial extent. For a BLR with either fixed or variable boundaries, four case studies may be considered: (i) fixed  $R_{\text{in}}$ , fixed  $R_{\text{out}}$  (the default scenario), (ii) variable  $R_{\text{in}}$ , fixed  $R_{\text{out}}$ , (iii) fixed  $R_{\text{in}}$ , variable  $R_{\text{out}}$ , and (iv) variable  $R_{\text{in}}$ , variable  $R_{\text{out}}$ . However, as already mentioned, when the surface area of the emitting region is taken into consideration, the low emission measure arising from gas at small BLR radii (for this geometry) suggests that a variable inner boundary has little impact on the overall emission-line response. We have confirmed this supposition via model simulations. Thus case (iii), variable

$R_{\text{out}}$ , and to a lesser extent case (iv), variable  $R_{\text{in}}$ ,  $R_{\text{out}}$ , are of primary interest here.

As before, we adopt the fiducial BLR model as our baseline model against which comparisons with dust-bounded BLR models will be made. The fiducial model is truncated at a fixed outer radius of 100 light-days, a distance beyond which there is no contribution to the total line emission. This we drive with our mock ionizing continuum light curve for NGC 5548, generating a model emission-line light-curve using the radial surface emissivity curve for  $\text{H}\beta$  (Figure 1b) from Korista and Goad (2004), and assuming a full non-linear response in the line. The fixed boundary model, equivalent to a dust bounded BLR for which the dust condensation and dust sublimation timescales are infinitely long, and for which the contribution to the total line emission of dusty clouds is set to zero (Figure 9, upper panel), serves as a point of reference. For each continuum–model emission-line light-curve pair, we compute the mean delay (CCF centroid and peak), and effective responsivity  $\langle \eta_{\text{eff}} \rangle$  over the full 13 yr light-curve, referenced to the mock driving continuum. We also report the range in measured delays and responsivity over time periods approximating the 13 seasons of data for this source<sup>13</sup>. The former may be compared with the range in responsivity-weighted radii measured from the centroid of the instantaneous 1-d response functions. Results for all of the simulated emission-line flux light curves presented in this work are summarised in Table 2.

### 6.1 A variable hard boundary model: $\tau_{\text{subl}}, \tau_{\text{cond}}$ small

For illustrative purposes only, we first consider what we here refer to as a variable hard boundary model for which the dust condensation and dust sublimation timescales are assumed to be small ( $\tau_{\text{cond}} = \tau_{\text{subl}} = 1$  day), i.e.  $R_{\text{out}}$  is tied to  $R_{\text{subl}}$ . For this model BLR clouds simply switch on/off once the continuum is of a sufficiently high/low level, a process which we consider to be unphysical. However, we include it here as it serves to illustrate the most extreme range in variability (i.e. it shows the largest range in  $R_{\text{eff}}$ ). Gas interior to the current location of  $R_{\text{subl}}$  will be fully emissive, while that beyond  $R_{\text{subl}}$  will emit at only 10% efficiency. Here  $R_{\text{subl}}$  acts as a sliding on-off switch for BLR clouds with the location of  $R_{\text{subl}}$  governed by the relation  $R_{\text{subl}} \propto C(t)^{1/2}$ .

Comparing Figure 9, panel (ii) (a dust-bounded BLR) with Figure 9 panel (i) (the fiducial fixed boundary model), illustrates a number of key attributes of a dust-bounded BLR. First, the range in delays, as measured from the seasonal data is considerably larger than for fixed boundary models. Note that the predicted range in responsivity-weighted radii is large  $27.1 < R_{\text{RW}}$  (light-days)  $< 55.5$ , indicating a BLR which is a factor 2 smaller in low continuum states than in high continuum states. Second, the time averaged effective responsivity is significantly larger ( $\eta_{\text{eff}} = 0.81$  c.f. 0.51) when compared to fixed boundary

<sup>13</sup> Here we define a season as extending from the last data point of the previous season to the first point of the following season inclusive. This has negligible effect on the measured seasonal lags while ensuring that when extrapolating the light-curves between seasonal gaps, the light-curve is well behaved.

models, and exceeds that measured for  $H\beta$  for the 13 yr monitoring campaign ( $\langle \eta_{\text{eff}} \rangle = 0.55$ , see Table 2). The BLR is more compact in low continuum states and responds more coherently and with larger amplitude than does a fixed boundary model of similar dimensions. Consequently, the variable boundary model is a far better match to low continuum states, for example epochs 400–600, and 1200–1400, than is a fixed boundary model. The mean delay at the start of the campaign is still too long however, possibly pointing to a more compact BLR geometry than that used here, or alternatively, a prolonged low continuum state, and thus a smaller  $R_{\text{subl}}$  prior to the start of the 13 yr campaign (see end of §6.2). However, the extreme variation in the location of the BLR outer boundary exhibited by this model is less successful at reproducing the emission-line response in the highest continuum states during the latter half of the 13 yr campaign (e.g. epochs 2000–4000). The larger surface area available at larger BLR radii for this geometry coupled with the relatively shallow radial surface emissivity distribution results in enhanced variability over and above that which is observed for broad  $H\beta$  during high continuum states, and when compared to models with fixed outer boundary. A variable “hard” outer boundary with  $\tau_{\text{cond}}, \tau_{\text{subl}}$  small, thus appears prohibited by the data.



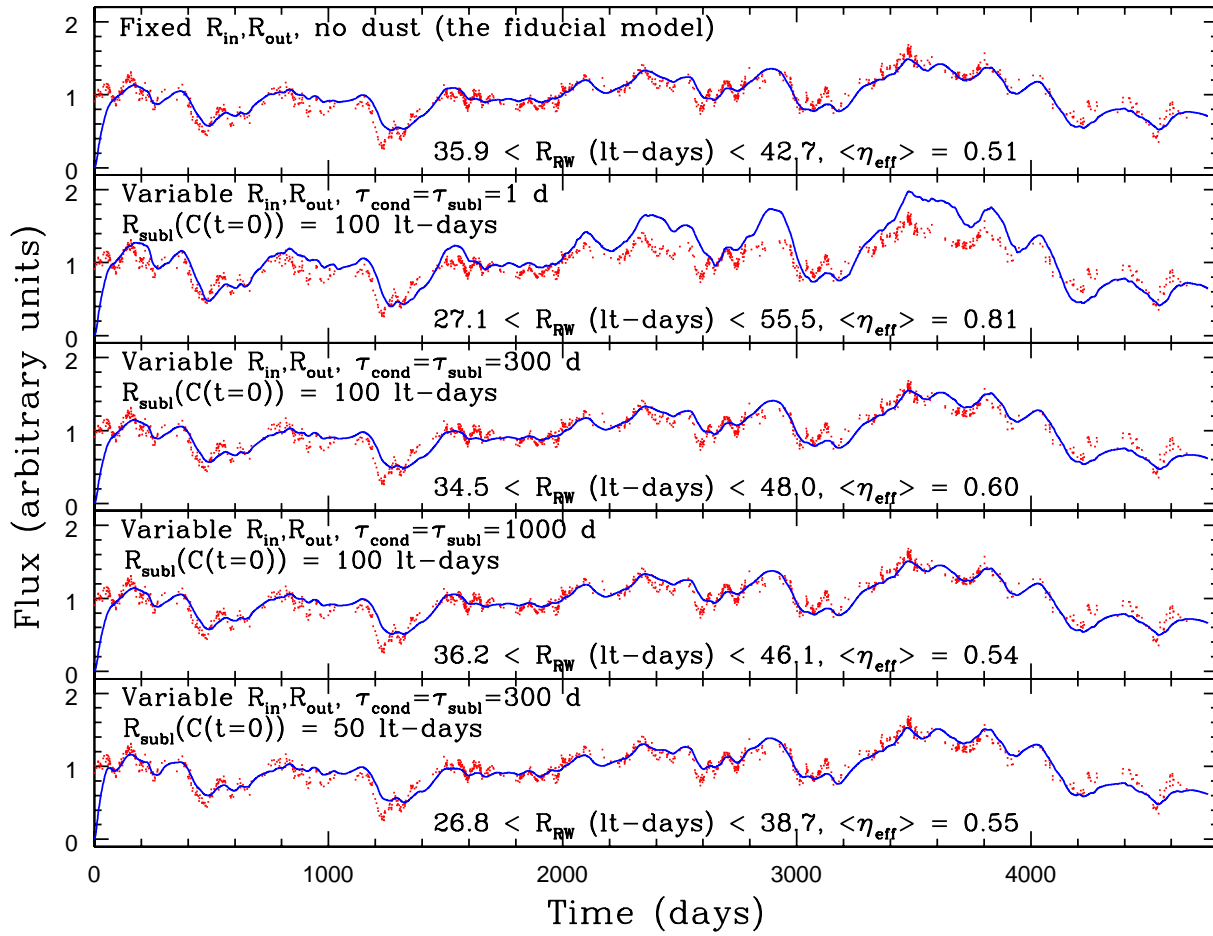


**Figure 9.** Model broad  $H\beta$  emission-line light-curves for NGC 5548 generated by driving the fiducial fixed boundary BLR model (upper panel) and variable dust bounded BLR models (panels 2–5) with the mock ionizing continuum. The observed  $H\beta$  light-curve is indicated in red, simulated light-curves in blue. Quoted values are for the simulated light-curves.



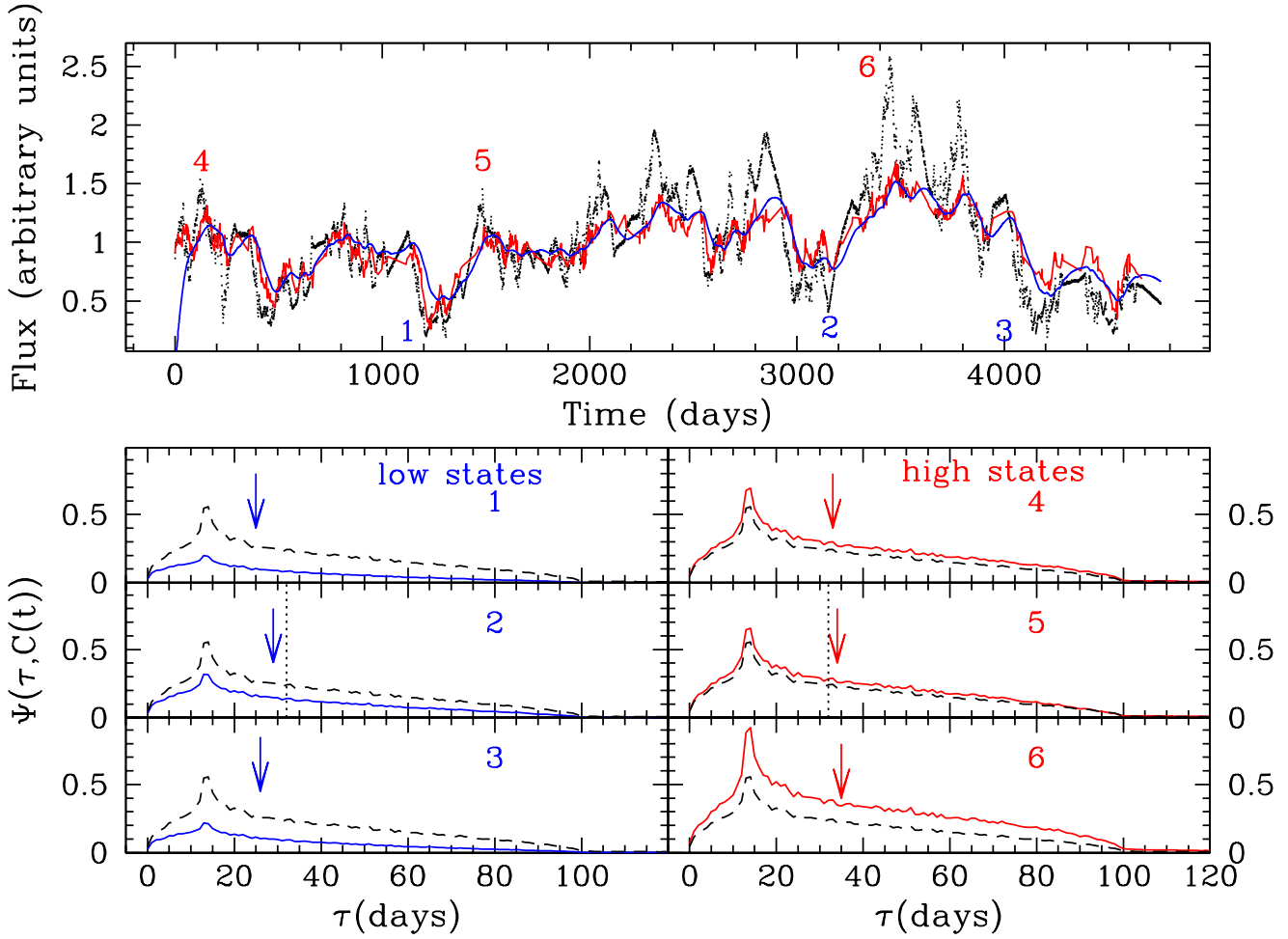


**Figure 10.** Upper panel - model continuum light curve (black dots), and observed (red line) and model broad  $H\beta$  (blue line) emission-line light curves for a dust-bounded model of NGC 5548 with  $\tau_{\text{cond}} = \tau_{\text{subl}} = 1000$  days. Lower panels - corresponding instantaneous time-dependent transfer functions  $\Psi(\tau, C(t))$ , for 3 low-states (panels 2-4, LHS, solid blue lines) and 3 high-states (panels 5-7, RHS, solid red lines). For reference the steady-state transfer function corresponding to a mean continuum of 1 is indicated by the dashed black line. The vertical arrows indicate the centroid of  $\Psi(\tau, C(t))$  at the corresponding epoch. For clarity, each has first been normalised to an arbitrary flux. Note that the centroid of  $\Psi(\tau, C(t))$  is large in high continuum states and small in low continuum states. The centroid of the steady state transfer function is indicated by the vertical dotted line in the middle 2 panels.

## 6.2 A soft (or “fuzzy”) BLR outer boundary

For the fiducial BLR geometry, a variable hard boundary model, while providing a better match to low continuum states, is found to be too responsive during high continuum states, producing variability over and above that which is observed. We now consider dust bounded models in which the dust condensation and dust sublimations timescales are comparable to, or significantly longer than, the characteristic timescale of the driving continuum light-curve. These we refer to as “soft” boundary models. Values of  $\tau_{\text{cond}}$ ,  $\tau_{\text{subl}}$  were chosen to be large enough to suppress the excessive variability exhibited by variable hard boundary models in high continuum states while still allowing significant changes in  $R_{\text{eff}}$  during low continuum states. We note in passing that as  $\tau_{\text{subl}}$  and  $\tau_{\text{cond}}$  increase, the effective BLR size and its response become increasingly sensitive to the long term history of the continuum variations. First, we consider a model with a starting dust sublimation radius of  $R_{\text{subl}} = 100$  light days and with  $\tau_{\text{subl}} = \tau_{\text{cond}} = 300$  days (Figure 9, panel (iii)), a factor few larger than  $\tau_{\text{max}}$  the maximum BLR delay at the starting outer radius, and a close approximation to the characteristic variability timescale of the mock driving continuum light-curve (Kelley et al. 2009). Figure 5 indicates that models for which  $\tau_{\text{subl}} = \tau_{\text{cond}}$  are characterised by symmetric excursions in line reprocessing efficiency  $\epsilon(r, t)$ . Thus the effective outer boundary will vary with continuum level with a delay set by the dust sublimation and dust condensation timescales.

Figure 9 panel (iii) shows that for  $\tau_{\text{subl}} = \tau_{\text{cond}} = 300$  days, the emission-line responsivity,  $\langle \eta_{\text{eff}} \rangle = 0.60$ , is somewhat larger than that measured over the 13 yr campaign ( $\langle \eta_{\text{eff}} \rangle = 0.55$ ), but importantly, significantly smaller than that measured for the variable hard boundary model. This general trend of decreasing emission-line variability amplitude with increased  $\tau_{\text{cond}}$ ,  $\tau_{\text{subl}}$  has been verified with simulations (e.g. compare Figure 9, panels (ii)–(iv), and see Table 2). The  $\text{H}\beta$  emission-line variability amplitude for  $\tau_{\text{subl}} = \tau_{\text{cond}} = 300$  days, is generally larger than is observed during high continuum states. This is a consequence of the line emitting region extending to include high responsivity gas at larger radii (see Fig 1b). Furthermore, with such long timescales for dust destruction and dust reformation, the range in spatial extent of the BLR  $34.5 < R_{\text{RW}} \text{ (light-days)} < 48.0$ , is found to be only marginally larger than that found for a model with static BLR boundaries ( $35.9 < R_{\text{RW}} \text{ (light-days)} < 42.7$ ).

With such large values for  $\tau_{\text{subl}}$  and  $\tau_{\text{cond}}$ , the spatial extent of the BLR will remain large on average except during prolonged periods (longer than the BLR light-crossing time) of low continuum flux. In the absence of prolonged low continuum states, a more compact BLR may be realised if  $\tau_{\text{cond}}$  is significantly shorter than  $\tau_{\text{subl}}$ . Under these circumstances, the BLR will become more compact during the decline toward lower continuum states but will not grow in size as quickly when transitioning toward higher continuum states (e.g., note the difference in the observed decline in  $F(r)$  (i.e.  $R_{\text{eff}}$ ) relative to the expected location of  $R_{\text{subl}}$  for the low (panel (iv)) and high (panel (vi)) continuum states shown in Figure 8). The BLR will thus be smaller on average than for a model in which  $\tau_{\text{cond}} \geq \tau_{\text{subl}}$ .

In Figure 9 panel (iv) we illustrate the effect of increas-

ing the dust condensation and dust sublimation timescales to 1000 days, which from dust reverberation mapping experiments, are thought to be representative of the likely macroscopic dust condensation and dust sublimation timescales in nearby AGN (Kishimoto et al. 2013; Schnülle et al. 2013, 2015). This model achieves the goal of suppressing excessive variability in high continuum states, and has a similar time-averaged responsivity ( $\langle \eta_{\text{eff}} \rangle = 0.54$ ) to the fixed boundary model, but at the expense of a smaller range in  $R_{\text{RW}}$  than models with smaller  $\tau_{\text{cond}}$ ,  $\tau_{\text{subl}}$ . For this model, large changes in the effective outer boundary will only become apparent for prolonged rises or falls in the ionizing continuum flux<sup>14</sup>.

With the caveat that we are here exploring the behaviour of only one of many possible BLR geometries, these simulations suggest that if the BLR is bounded by dust at its outer edge, then dust condensation and sublimation timescales must be comparable to, or significantly longer than the characteristic timescale of the driving continuum light-curve  $T_{\text{char}}$ , so that  $R_{\text{eff}}$  remains approximately constant (e.g. compare panels (i) and (iv) of Figure 9). We note that none of the dust-bounded simulations discussed so far are particularly successful at matching the observed line behaviour during the low continuum state at 1200 days. Either the BLR is more compact than that described here, or  $\tau_{\text{cond}}$  may be significantly shorter than  $\tau_{\text{subl}}$ .

In the bottom panel of Figure 9 we simulate the emergence from a prolonged low continuum state prior to the start of the campaign, setting the starting dust sublimation radius  $R_{\text{subl}}(C(t) = 0)$  to 50 light-days, for a dust-bounded BLR for which the dust sublimation and dust condensation timescales are 300 days. This model was motivated by the relatively poor match of previous models to the first very low continuum state (epochs 1200-1400), i.e. at the start of the campaign the BLR responds too slowly (the delays are too large), and the amplitude of response is a poor match to the observed emission-line strength during low continuum states. If prior to the onset of the 13 yr ground-based monitoring campaign, the BLR had been in an extended low-state, then it is at least plausible that the dust extended to far smaller BLR radii than that considered here. This model exhibits some promising characteristics. The variability timescale is in general smaller than that for a static boundary model  $26.8 < R_{\text{RW}} \text{ (light-days)} < 38.7$ , while the variability amplitude remains high  $\langle \eta_{\text{eff}} \rangle = 0.55$ , though marginally less than that shown by a model with a larger initial radius for the hot dust (Figure 9 panel (iii)). It is also a better match to the observed short timescale variability and to the observed variability in high continuum states than a fixed boundary model with  $R_{\text{out}} = 50$  light-days (Figure 4, panel (iv)). However for such a small BLR, the  $\text{H}\beta$  luminosity remains an issue.

In Figure 10 we compare the instantaneous continuum level dependent transfer functions,  $\Psi(\tau, C(t))$ , for a dust-bounded BLR, with  $\tau_{\text{cond}} = \tau_{\text{subl}} = 1000$  days, as deter-

<sup>14</sup> We note that long dust sublimation and dust condensation timescales will introduce a memory into the system behaviour (other than that attributed to reverberation effects within the spatially extended BLR) that may persist well beyond the characteristic timescale of the driving continuum light-curve or indeed the maximum delay at the BLR outer radius.

mined for a selection of low- (solid blue curve) and high- (solid red curve) continuum states over the 13 yr campaign. The centroid of  $\Psi(\tau, C(t))$  is indicated by the coloured arrows. The dotted vertical line indicates the centroid of the transfer function for the steady-state (i.e.  $\Psi(\tau, C(t) = 1)$ , dashed black curve). The amplitude and centroid of the continuum-level-dependent transfer function are larger in high continuum states and smaller in low-continuum states. Note that even though the low continuum states (labelled 1–3), are similar in flux, the transfer functions (shown in blue) display significant differences. This is a consequence of differences in the prior continuum history which can lead to differences in the effective BLR size in the presence of dust for the same continuum level.

The general trend of decreased variability amplitude (particularly in high-continuum states) with increasing  $\tau_{\text{cond}}$ ,  $\tau_{\text{subl}}$ , suggests that if the BLR is bounded by dust, then the dust sublimation and dust condensation timescales are long when compared to the BLR “size” and characteristic timescale of the driving continuum. Kishimoto et al. (2013) recently reported direct evidence for a receding dust sublimation region, using near-IR interferometry of the nearby type I AGN, NGC 4151. They find that the size of the near-IR emitting region scales with the long-term average UV/optical continuum flux, brightening with a delay relative to the UV/optical continuum on timescales of a few years. This suggests that the macroscopic dust sublimation timescale is at least of order a few years in duration in this object in line with our simulations. Similarly, in an independent study Schnülle et al. (2013) found that the radiation from the hot dust in NGC 4151 brightens as the continuum increases with a delay of  $\sim 50$  days. They suggest that the hot dust is cooler than the sublimation temperature and therefore lies beyond the dust sublimation radius and is fairly robust to destruction by UV photons on short timescales, again pointing toward a rather static dust distribution.

In summary, while allowing the location of the BLR outer boundary to vary in response to continuum variations has some obvious advantages (allowing a more compact BLR in low continuum states and a larger BLR in high continuum states), these (advantages) are mitigated by the excess variability produced during high continuum states. Our simple toy model suggests that dust can suppress the variable contributions to the line emission from the outer BLR, provided that the dust sublimation timescales are long. These simulations therefore appear to favour a BLR outer boundary which is robust to significant continuum variations (i.e. a static BLR outer boundary).

### 6.3 What limits the BLR outer radius?

The radial extent of the BLR is a key quantity because it defines the volume within which the emission-line luminosity and variability must ultimately be derived. The BLR must be sufficiently large to reprocess a substantial fraction of the source ionizing luminosity, but cannot extend to arbitrarily large radii. The velocities at large radii, and indeed the line-emissivities arising from such gas, would be small enough that the emission-lines (if present) would be weak and narrow. For the fiducial geometry described here, the BLR outer boundary has been set by the distance at

which dust grains can form (i.e. the location of the hot dust). This choice was informed by reverberation mapping of multiple broad emission-lines and dust within individual sources, which suggest that the line emitting region extends at least as far as the expected location of the hot dust (Clavel et al. 1991; Krolik et al. 1991; Peterson et al. 2002, Barth et al. 2011; Koshida et al. 2014). Moreover, since the BLR and ultimately the accretion disc are likely supplied by the reservoir of gas residing in the dusty torus, scenarios in which there exists a substantial physical gap between the outer BLR and the inner edge of the dusty torus seem physically less attractive.

While the observable line-emitting gas in the fiducial model is approximated to lie along the surface of a bowl (which has a large covering fraction for polar angles greater than 50 degrees), we do not exclude the possibility that this surface may be “patchy” and that gas located at significant depth behind the surface may also contribute to the observed line emission. These shielded clouds will be exposed to a heavily filtered ionizing continuum, and so may reside in an environment suitable for significant dust formation. The fiducial model geometry is limited in extent along the upper reaches of the bowl-surface by dust and, by construction, behind the surface by severe cloud–cloud shadowing (and/or dust). These effects may be also important in limiting the BLR spatial extent for other very different BLR geometries, or alternatively, the BLR could simply be gas bounded.

## 7 DISCUSSION AND SUMMARY

In paper I we showed that for model BLRs of varying size and fixed boundaries, that the measured emission-line responsivity and delay are correlated, for characteristic timescales of the driving continuum light curve which are less than the maximum delay at the BLR outer radius. This we attributed to geometric dilution arising from reverberation effects within the spatially-extended BLR which act to reduce the emission-line responsivity and delay from their expected values, but in a predictable way. Next, we showed that the measured emission line responsivity and delay are sensitive to the duration of the monitoring campaign, and less so on sampling rate (for a randomly sampled light curve). Significantly, we also found that in order to satisfy the observed *intrinsic* Baldwin Effect (Kinney, Rivolo, and Koratkar 1990; Pogge and Peterson 1992; Gilbert and Peterson 2003; Goad, Korista, and Knigge 2004; Kong et al. 2006), and reproduce the observed strong positive correlation between BLR size and luminosity in a single source (Peterson et al. 2003; Cackett et al. 2006), the line radial surface emissivity distribution  $F(r)$  must steepen toward larger BLR radii.

In the present work, we deliberately focused our attention on the nature of the BLR outer boundary,  $R_{\text{out}}$ , and in particular its location in the presence of ionizing continuum flux variations, since  $R_{\text{out}}$  sets the volume within which the total luminosity and time variable nature (i.e., characteristic size and responsivity) of the emission lines is determined. This is especially true of emission lines that form at larger BLR radii (e.g.,  $H\beta$  and  $Mg\ II$ ), which are often used in scaling relationships applied to black hole mass determinations at high redshift (McLure and Jarvis 2002; Vestergaard and Peterson 2006; Bentz et al. 2009; Kileci Eser et al. 2015).

However, the physical mechanism that sets the BLR outer boundary remains uncertain. It may be photon limited, dust-bounded or simply truncated (i.e., one that cuts-off due to a particular geometrical arrangement of gas). It is often assumed that the location of  $R_{\text{out}}$  is set by the dust sublimation radius, heretofore with little or no consideration for what might happen to this boundary when the incident continuum varies. In keeping with the idea that the BLR extends from the outer accretion disc to the inner edge of the duty torus (Netzer and Laor 1993; Nenkova et al. 2008; Mor and Trakhtenbrot 2011; Mor and Netzer 2012; Goad, Korista and Ruff 2012), we here have explored the effects of imposing a dust-bounded BLR on  $L$ ,  $R_{\text{RW}}$  and  $\eta$  for a particular emission line,  $\text{H}\beta$ . Observationally, the location of the hot dust has been shown to vary with continuum luminosity, both within an individual AGN and among the AGN population as a whole (Suganuma et al. 2004, 2006; Koshida et al. 2014). Thus, in the present work, we have also considered a time-variable location for the BLR outer boundary in response to continuum variations. With this aim we constructed a mock ionizing continuum light curve using the best available optical continuum light curve from the 13 yr ground-based monitoring campaign of NGC 5548, to drive emission line variations (see §2.2).

With reference to the best-studied AGN, NGC 5548, if dust limits the spatial extent of the BLR, significant correlations between the continuum level and the effective outer boundary of the BLR are ruled out, because the emission line lags become far too long and the gas becomes overly responsive in the higher continuum states. Dust-bounded BLR models therefore favour dust sublimation and condensation timescales which are large compared to both the BLR light crossing time and the characteristic variability timescale of the driving continuum, also favoured in dust-reverberation experiments (Hönig and Kishimoto 2011; Kishimoto et al. 2011, 2013; Schnülle et al. 2013, 2015).

A static BLR imposes strong constraints upon the physical properties of the line emitting gas. With an outer boundary set by the graphite sublimation radius, the BLR model is underluminous in  $\text{H}\beta$  by a factor 2, and the delays are too large. Furthermore, although the model response amplitude of  $\text{H}\beta$  is a good approximation to the observed time-averaged value, the model emission-line light curve is a poor approximation to the observed flux variations during the lowest continuum states.

The emission line delays may be reduced on average by choosing a smaller cut-off for the BLR outer boundary (i.e.,  $R_{\text{out}} \ll R_{\text{subi}}$ ). However, this leads to a still lower predicted luminosity, as well as a smaller amplitude response in  $\text{H}\beta$  despite the BLR being more compact<sup>15</sup>. This smaller amplitude response arises because the gas with largest responsivity, usually associated with low incident ionizing continuum fluxes and equated with larger BLR radii, is no longer

present. This is an illustration of the strong tensions between  $L$ ,  $R_{\text{RW}}$ ,  $\eta$  for a particular emission line. Since these three quantities are encapsulated in the emission line transfer function, an understanding of the tensions between them may prove useful in the interpretation of velocity-resolved delay signatures recovered from reverberation mapping experiments. They may also be used to inform the continued development of forward modelling techniques, recently employed to map the geometry and kinematics of the BLR gas and constrain black hole masses.

We also found that in general, a lower continuum normalisation provides a better match to the emission-line delays and responsivities (e.g., Figure 4, panels (ii) and (iii)), with the caveat that the predicted  $\text{H}\beta$  emission line luminosities for these models remain too small (see Tables 1 and 2 for details). Since large uncertainties in the luminosity distance to NGC 5548 are unlikely, these simulations may point toward another mechanism for altering the mapping of  $\Phi_{\text{H}}$  onto  $r$ , i.e., a smaller  $\Phi_{\text{H}}$  for a given  $r$  than that inferred from the observed UV continuum flux and typical models of the continuum SED. As an alternative, we investigated various ways of boosting the  $\text{H}\beta$  emissivity  $F(r)$  and responsivity  $\eta(r)$  at smaller BLR radii, which resulted in a reduction in the responsivity-weighted radius without requiring changes in the BLR geometry (see §4, Figure 3a,b and Table 1).

The physical size of the BLR is determined in large part by the energy deposited into and reprocessed by the system. The luminosity-weighted radius of a given emission line is dictated by the distribution of the continuum reprocessing efficiency for that line and the distribution of cloud solid angle intercepting the ionizing photons. That the energy deposited is important in constraining the line-emitting geometry, is amply demonstrated in Horne, Korista and Goad (2003, their Figures 5, 6). They show that even for a single cloud model, whose reverberation signature is described by a paraboloidal iso-delay surface (for which the cloud-source distance is unconstrained), the correct radial distance may be recovered if the emitted energy in the emission line is properly accounted for, for a specified incident ionizing continuum flux. The connection between energy and BLR size is also revealed through the *remarkably tight observed relation* between the measured characteristic time-delay  $\tau(\text{H}\beta)$  (interpreted as  $R_{\text{BLR}}/c$ ) and the observed luminosity (Bentz et al. 2013; Kilerci Eser et al. 2015). The physical size scale for the BLR is also revealed through the mass of the central black hole  $M_{\text{BH}}$ , via the virial relation  $v^2 R_{\text{BLR}} \propto M_{\text{BH}}$ , although  $R_{\text{BLR}}$  is again inferred from the continuum-emission-line delay information. Without additional information (e.g., energy),  $R_{\text{BLR}}$  remains degenerate in delay.

Finally, that the majority of features observed in the 13 yr  $\text{H}\beta$  emission-line light curve are captured in the simulations (see Figure 4, panel (iii)) validates use of the scaled optical (or equivalently the UV) continuum as a proxy for the driving ionizing continuum. It also demonstrates the power of photoionization models for gaining an understanding of the BLR.

<sup>15</sup> A weak correlation between the continuum and the emission-line variations does not necessarily imply a large BLR. Rather, in the absence of significant geometric dilution it may be indicative of low reprocessing efficiency for that emission line (e.g. Mg II). This may in part explain the difficulty in obtaining an accurate lag estimate for this line (see e.g., Clavel et al. 1991; Krolik et al. 1991; Cackett et al. 2015).

**Table 2.** H $\beta$  emission-line delays (CCF peak, CCF centroid) and time-averaged responsivities for the full 13 yr light-curve (columns 2–4), and for the seasonal light-curves (columns 5–8), see text for details.

|  | $CCF_{\text{peak}}$<br>(days) | $CCF_{\text{cent}}^*$<br>(days) | $\langle \eta_{\text{eff}} \rangle^\dagger$ | $CCF_{\text{cent}}$ (range) $^\ddagger$<br>(days) | $R_{\text{LW}}$<br>(light-days) | $R_{\text{RW}}$<br>(light-days) | $\eta_{\text{eff}}$ (range) |
|--|-------------------------------|---------------------------------|---|---|---------------------------------|---------------------------------|-----------------------------|
| observations   | $17.3 \pm 1.4$                | $35.6 \pm 1.7$                  | 0.55  | 12.4 – 27.0                                       | NA                              | NA                              | 0.3 – 0.99                  |
| $R_{\text{out}} = 100$ light-days, fixed boundaries  |                               |                                 |   |   |                                 |                                 |                             |
| power-law, $\gamma = -2$   | $10.0 \pm 0.5$                | $18.2 \pm 1.5$                  | 0.97  | 6 – 15.2  | 15.8                            | 15.8                            | 0.70 – 1.12                 |
| power-law, $\gamma = -1$   | $25.8 \pm 3.7$                | $36.6 \pm 1.2$                  | 0.46  | 17.3 – 33.4                                       | 33.6                            | 33.6                            | 0.30 – 0.46                 |
| Fiducial LOC model   | $38.9 \pm 2.1$                | $43.5 \pm 1.4$                  | 0.51  | 23.9 – 42.5                                       | 31.2 – 38.4                     | 35.9 – 42.7                     | 0.30 – 0.54                 |
| LOC low continuum normalisation  | $36.3 \pm 1.9$                | $41.5 \pm 1.3$                  | 0.60  | 25.7 – 40.0                                       | 26.5 – 36.2                     | 31.8 – 41.1                     | 0.35 – 0.67                 |
| LOC high continuum normalisation   | $39.6 \pm 2.3$                | $44.1 \pm 1.4$                  | 0.43  | 23.8 – 46.2                                       | 34.9 – 39.5                     | 38.0 – 42.5                     | 0.23 – 0.45                 |
| $R_{\text{out}} = 50$ light-days, fixed boundaries   |                               |                                 |   |   |                                 |                                 |                             |
| LOC model  | $22.8 \pm 0.8$                | $29.8 \pm 1.4$                  | 0.42  | 21.2 – 29.0                                       | 21.4 – 23.9                     | 23.1 – 25.6                     | 0.30 – 0.49                 |
| LOC model  | $17.9 \pm 1.0$                | $24.2 \pm 1.4$                  | 0.53  | 18.7 – 28.6                                       | 15.4 – 18.9                     | 17.7 – 21.1                     | 0.43 – 0.67                 |
| log $\Phi_{\text{H}} = 20$ at $R = 7.5$ light-days   |                               |                                 |   |   |                                 |                                 |                             |
| Dusty BLR, $R_{\text{max}} = 200$ light-days, $R_{\text{subl}} = 100$ light-days, variable boundaries      |                               |                                 |   |   |                                 |                                 |                             |
| $\tau_{\text{subl}} = \tau_{\text{cond}} = 1$ days   | $57.9 \pm 3.5$                | $66.6 \pm 2.5$                  | 0.81  | 38.1 – 123.3                                      | 23.1 – 49.2                     | 27.1 – 55.5                     | 0.10 – 0.84                 |
| $\tau_{\text{subl}} = \tau_{\text{cond}} = 300$ days   | $45.7 \pm 2.3$                | $53.0 \pm 1.8$                  | 0.60  | 25.4 – 52.5                                       | 29.7 – 42.4                     | 34.5 – 48.0                     | 0.21 – 0.62                 |
| $\tau_{\text{subl}} = \tau_{\text{cond}} = 1000$ days  | $41.9 \pm 2.5$                | $47.1 \pm 1.4$                  | 0.54  | 24.8 – 46.3                                       | 31.2 – 40.7                     | 36.2 – 46.1                     | 0.26 – 0.58                 |
| Dusty BLR, $R_{\text{out}} = 200$ light-days, $R(\tau_{\text{subl}}) = 50$ light-days, variable boundaries |                               |                                 |   |   |                                 |                                 |                             |
| $\tau_{\text{subl}} = \tau_{\text{cond}} = 300$ days   | $33.4 \pm 2.0$                | $47.3 \pm 1.7$                  | 0.55  | 23.8 – 48.1                                       | 22.6 – 32.4                     | 26.8 – 38.7                     | 0.24 – 0.60                 |

\* CCF centroids have been calculated over the range in delays for which the CCF coefficient  $> 0.8$  of the peak value. Quoted values and their uncertainties have been determined using the model-independent FR/RSS Monte Carlo method described in Peterson et al. (1998). Each model light-curve is first sampled in the same fashion as the observations. We then compute 1000 realisations of each light-curve, assuming random sampling, with full replacement. Errors on individual data points have been drawn from a random Gaussian deviate with dispersion of 1% of the measured flux.

$\dagger \langle \eta_{\text{eff}} \rangle$  values are here determined as in Goad et al. (2004), from the ratio  $d \log F_{\text{line}} / d \log F_{\text{cont}}$ .

$\ddagger$  Measured ranges have been determined from measurements of each of the 13 seasons of data for NGC 5548.

## 8 ACKNOWLEDGEMENTS

We would like to thank the anonymous referee for providing many insightful suggestions which have led to improved clarity of the work presented here. Mike Goad would like to thank the generous hospitality of Kirk and Angela Korista and the Department of Physics & Astronomy at Western Michigan University during the initial stages of this work. Kirk Korista would like to thank the University of Leicester for their hospitality during the completion of this work.

## 9 REFERENCES

- Ade, et al. 2014, *A&A* 61, A16.
- Baldwin, J. Ferland, G., Korista, K., and Verner, D. 1995, *ApJ* 455, 119.
- Barth, A.J., Pancoast, A., Bennert, V.N. et al. 2013, *ApJ* 769, 128.
- Barth, A.J., Pancoast, A., Thorman, S.J. et al. 2011, *ApJ* 743, 4.
- Barvainis, R. 1987, *ApJ* 320, 537.
- Bentz, M.C., Denney, K.D., Grier, C.J. et al. 2013, *ApJ* 767, 149.
- Bentz, M.C., Horne, K., Barth, A.J. et al. 2010 *ApJ* 720, 46.
- Bentz, M. and Katz, S. 2015, *PASP* 127, 67.
- Bentz, M., Peterson, B.M., Netzer, H., Pogge, R.W., and Vestergaard, M. 2009a, *ApJ* 697, 160.
- Bentz, M.C., Walsh, J.L., Barth, A.J. et al. 2009b, *ApJ* 705, 199.
- Bentz, M., Walsh, J.L., Barth, A.J. et al. 2008, *ApJ* 689, 21.
- Bentz, M.C., Denney, K.D., Cackett, E.M. et al. 2007, *ApJ* 662, 205.
- Bentz, M.C., Peterson, B.M., Pogge, R.W. et al. 2006, *ApJ* 644, 133.
- Blandford, R.D. and McKee, C.F. 1982, *ApJ* 255, 419.
- Bottofrff, M.C., Baldwin, J.A., Ferland G.J. et al. 2002, *ApJ* 581, 932.
- Bottofrff, M., Ferland G., Baldwin, J. and Korista, K. et al. 2000, *ApJ* 542, 644.
- Cackett, E.M. and Horne, K. 2006, *MNRAS* 365, 1180.
- Cackett, E.M., Gultekin, K., Bentz, M. C., et al. 2015, [arXiv:1503.02029](https://arxiv.org/abs/1503.02029).
- Chiang, J., Reynolds, C.S., Blaes, O.M. et al. 2000, *ApJ* 528, 292.
- Clavel, J. Reichert, G.A. Alloin, D. et al. 1991, *ApJ* 366, 64.
- Collin-Souffrin, S. 1986 *A&A* 166, 115.
- Collin, S., Kawaguchi, T., Peterson, B.M. and Vestergaard, M. 2006 *A&a* 456, 75.
- Davidson, K. and Netzer, H. 1979, *Rev. Mod. Phys.* 51, 715.
- Denney, K. D., Peterson, B. M., Pogge, R. W., et al. 2010, *ApJ* 721, 715.
- Denney, K. D., Peterson, B. M., Pogge, R. W., et al. 2009, *ApJ* 704, 80.
- Kilerci Eser, E. Vestergaard, M. Peterson, B.M. et al. 2015, *ApJ* 801, 8.
- Ferland, G.J., Korista, K. T., Verner, D. A. et al. 1998, *PASP* 110, 761
- Ferland, G. J., Korista, K. T. and Verner, D. A. 1997, In: *Astronomical Data Analysis Software and Systems VI*, A.S.P. Conference Series, Vol. 125, 1997, Gareth Hunt and H. E. Payne, eds., p. 213.
- Ferland, G. J., Korista, K. T., Verner, D. A., Ferguson, J. W., Kingdon, J. B. and Verner, E. M. 1998, In: *The Publications of the Astronomical Society of the Pacific*, Volume 110, Issue 749, pp. 761-778.
- Ferland, G.J., Peterson, B.M., Horne, K. Welsh, W.F., Nahar, S.N. 1992, *ApJ* 387, 95.
- Ferland, G. and Netzer, H. 1979, *ApJ* 229, 274.
- Gaskell, C.M. and Peterson, B.M. 1987, *ApJS* 65, 1.
- Gilbert, K.M. and Peterson, B.M. 2003, *ApJ* 587, 123.
- Goad, M.R. and Korista, K.T. 2014, *MNRAS* 444, 43.
- Goad, M. R.; Korista, K. T. and Ruff, A.J. 2012, *MNRAS* 426, 3086.
- Goad, M. R.; Korista, K. T.; Knigge, C., 2004, *MNRAS* 352, 277.
- Grier, C., Peterson, B.M., Horne, K. et al. 2013, *ApJ* 764, 47.
- Hönig, S.F. and Kishimoto, M. 2011, *A&A* 534, 121.
- Horne, K., Korista, K.T. and Goad, M.R. 2003, *MNRAS* 339, 367.
- Horne, K., Welsh, W.F. and Peterson, B.M. 1991, *ApJ* 367, 5.
- Kong, M.-Z., Wu, X.-B, Wang, R. Liu, F.K. and Han, J.L. 2006, *A&A* 456, 473.
- Kaspi, S. and Netzer, H. 1999, *ApJ* 524, 71.
- Kelly, B.C., Bechtold, J., Siemiginowska, A. 2009, *ApJ* 698, 895.
- Kinney, A.L., Rivolo, A.R. and Koratkar, A.P. 1990, *ApJ* 357, 338.
- Kishimoto, M., Hönig, S.F., Antonucci, R. et al. 2013 *ApJ* 775, 36.
- Kishimoto, M., Hönig, S. F., Antonucci, R., Millour, F. Tristram, K. R. W., and Weigelt, G. 2011, *A&A* 536, 78.
- Korista, K., Ferland, G. and Baldwin, J. 1997, *ApJ* 487, 555.
- Korista, K., Baldwin, J., Ferland, G., and Verner, D. 1997, *ApJS* 108, 401.
- Korista, K.T., Alloin, D., Barr, P. et al. 1995, *ApJS* 97, 258.
- Korista, K.T. and Goad, M.R. 2004, *ApJ* 606, 749.
- Korista, K.T. and Goad, M.R. 2001, *ApJ* 553, 695.
- Korista, K.T. and Goad, M.R. 2000, *ApJ* 536, 284.
- Koshida, S., Minezaki, T., Yoshii, Y. et al. 2014, *ApJ* 788, 159.
- Koshida, S., Yoshii, Y., Kobayashi, Y. et al. 2009, *ApJ* 700, 109.
- Krause, M., Schartmann, M. and Burkert, A. 2012, *MNRAS* 425, 3172.
- Krolik, J.H., Horne, K., Kallman, T.R. et al. 1991, *ApJ* 371, 541.
- Kuehn, C.A., Baldwin, J.A., Peterson, B.M. and Korista, K.T. 2008, *ApJ* 673, 69.
- MacLeod, C.L., Ivezić, Z., Kochanek, C.S. et al. 2010, *ApJ* 721, 1014.
- Maoz, D., Netzer, H., Peterson, B.M. et al. 1993, *ApJ* 404, 576.
- Marshall, H.L., Carone, T.E., Peterson, B.M. et al. 1997, *ApJ* 479, 222.
- Mathews, W.G. and Ferland, G.J. 1987, *ApJ* 323, 456.
- Mathews, W.G. 1982, *ApJ* 252, 39.
- McLure, R.J. and Jarvis, M.J. 2002, *MNRAS* 337, 109.
- Mor, R., and Trakhtenbrot, B. 2011, *ApJ* 737, L36.
- Mor, R. and Netzer, H. 2012, *MNRAS* 420, 526.
- Mushotzky, R.F., Edelson, R., Baumgartner, W. and Gandhi, P, *ApJ* 2011, 743, 12.

- Nemmen, R.S. and Brotherton, M.S. 2010, MNRAS 408, 1598.
- Nenkova, M., Sirocky, M.M., Nikutta, R. et al. 2008, ApJ 685, 160.
- Netzer, H. and Laor, A. 1993, ApJ 404, 51.
- Netzer, H. 1985, ApJ 289, 451.
- Netzer, H. 1987, MNRAS, 225, 55.
- O'Brien, P.T. Goad, M.R. and Gondhalekar, P.M. 1994, MNRAS 268, 845.
- Pancoast, A., Brewer, B.J., Treu, T. et al. 2012, ApJ 754, 49..
- Pancoast, A., Brewer, B.J., Treu, T. et al. 2014a MNRAS 445, 3073
- Pancoast, A., Brewer, B.J., Treu, T. 2014b MNRAS, 445, 3055.
- Pérez, E, Robinson, A. and de La Fuente, L. 1992, MNRAS 256, 103.
- Peterson, B.M., Denney, K.D., De Rosa, G. et al. 2013, ApJ 2013, 779, 109.
- Peterson, B.M., Ferrarese, L., Gilbert, K. M., Kaspi, S., Malkan, M. A., et al. 2004, ApJ 613, 682.
- Peterson, B.M. Berlind, P. Bertram, R. Bischoff, K., Bochkarev, N.G. et al. 2002 ApJ 581, 197.
- Peterson, B.M. and Wandel, A. 2000, ApJ 540, 13.
- Peterson, B.M., Wanders, I., Horne, K, et al. 1998, PASP 110, 660.
- Pogge, R.W. and Peterson, B.M. 1992, AJ, 103, 1084.
- Romanishin, W., Balonek, T.J. Ciardullo, R. et al. 1995, ApJ 455, 516.
- Schlafly, E.F. and Finkbeiner, D.P. 2011, ApJ 737, 103.
- Schnülle, K., Pott, J.-U., Rix, H.-W. et al. 2013, A&A 557, L13.
- Schnülle, K., Pott, J.-U., Rix, H.-W. et al. 2015, A&A 578, 57.
- Skielboe, A., Pancoast, A., Treu, T. et al. 2015, arXiv:1502.02031.
- Suganuma, M., Yoshii, Y., Kobayashi, Y. et al. 2006, ApJ 639, 46.
- Suganuma, M., Yoshii, Y., Koboyashi, Y. et al. 2004, ApJ 612, 113.
- Vestergaard, M and Peterson, B.M. 2006, ApJ 641, 689.
- Vestergaard, M and Peterson, B.M. 2005, ApJ 625, 688.
- Welsh, W.F. and Horne, K. 1991, ApJ 379, 586.